Journal of Advanced Ceramics
2024, **13**(12): 2051–2067
https://doi.org/10.26599/JAC.2024.9221000

Research Article

Superior thermal and oxygen barrier properties of high-entropy ferroelastic rare earth tantalate $(8RE_{1/8})TaO_4$

Jun Wang[1], Yongpan Zeng[2], Xiaoyu Chong[1], Manyu Zhang[1], Qianqian Jin[3], Yanjun Sun[2], Xiangwei Tang[2], Peng Wu[1,✉], Jing Feng[1,✉]

[1] *Faculty of Materials Science and Engineering, Kunming University of Science and Technology, Kunming 650093, China*
[2] *Guangdong Midea Kitchen Appliances Manufacturing Co., Ltd., Midea Group, Foshan 528300, China*
[3] *Materials Science and Engineering Research Center, Guangxi University of Science and Technology, Liuzhou 545006, China*

Received: May 1, 2024; Revised: November 2, 2024; Accepted: November 13, 2024

Abstract: Thermal/environmental barrier coatings (T/EBCs) are used to protect hot-section superalloys and/or ceramic matrix composite components from hot corrosion and oxidation; however, the majority of T/EBCs exhibit extremely high thermal and ionic conductivities. Here, we obtain a novel rare-earth tantalate with excellent oxygen and thermal insulation via a high-entropy strategy. The high-entropy component $(8RE_{1/8})TaO_4$ (RE = rare earth), which is designed by large size disorder and mass disorder, has been reassembled into a stabilized monoclinic structure. $(8RE_{1/8})TaO_4$ had 30.0%–31.1% and 59.2%–67.5% lower intrinsic thermal conductivity than single-RE $RETaO_4$ and $8(Y_2O_3–ZrO_2)$ 8YSZ at 1200 °C, respectively, and exhibited lower intrinsic thermal conductivity across the entire temperature range of 100–1200 °C. This is the result of strong scattering by the phonon–phonon, grain boundary, domain boundary, dislocation, and vacancy defects. The ionic conductivity of $(8RE_{1/8})TaO_4$ is 3712–29,667 times lower than that of 8YSZ at 900 °C, benefiting from the strong Ta–O bonding strength, low concentration of mobile oxygen vacancies and severe lattice distortions that impede carrier transport. Moreover, $(8RE_{1/8})TaO_4$ had superior high-temperature stability and excellent mechanical properties. Analysis of above results demonstrates that $(8RE_{1/8})TaO_4$ is a promising candidate for T/EBCs.

Keywords: thermal/environmental barrier coatings (T/EBCs); rare-earth tantalate; high entropy; thermal conductivity; ionic conductivity

1 Introduction

Thermal/environmental barrier coatings (T/EBCs) are widely used in aircraft engines and power-generation gas turbines to protect hot-section superalloys and/or ceramic matrix composite components from hot corrosion and oxidation [1–3]. There are four primary constituents in a T/EBC system: (i) the ceramic top coat (TC); (ii) a bond coat (BC) between the substrate and the TC, where the compositions of BC in typical TBCs and EBCs are generally MCrAlY (M = Ni, Co) and Si, respectively; (iii) a thermally grown oxide (TGO), predominantly alumina in TBCs and silica in EBCs, which forms between the TC and the BC; (iv) the superalloy substrate or ceramic matrix composite [4,5]. The TC provides oxidation and thermal protection for BC and substrate, and the BC can reduce the oxidation rate of metallic substrate and enhance the adherence between the substrate and top coat. TGO is a reaction product of BC oxidation by molecular forms of O_2 and H_2O or ionic forms of O^{2-} and OH^- anions [6,7]. The TGO overgrowth led to stresses and thermal mismatch stresses; eventually, cracking was found within the TGO and along the interfaces, which caused spallation and even failure of T/EBCs [8–10].

To address this issue, researchers have discovered that multilayer structural coating materials exhibit better anti-oxidation and thermal insulation properties than single-layer coatings [11,12]. However, the introduction of different materials will exacerbate the thermal mismatch problem and slightly improves the oxygen barrier properties. Additionally, researchers have endeavored to reduce the oxidation rate of the matrix through utilization of dense coatings, which impedes only the transport of O_2 and H_2O molecules via the pores in the coating, and the oxidation rate of matrix is still considerably high because of the high ionic conductivity of these coating materials [8,13,14]. Therefore, it is desirable to restrict the rate of O^{2-} and OH^- diffusion in dense structural coatings, and it is important to use the ionic conductivity as an indicator of the rate of carrier migration in the material to prolong the service life of T/EBCs. $Y_2O_3–ZrO_2$ (YSZ) is a common T/EBC material used in turbine blades [15,16]. However, YSZ cannot provide sufficient protection for substrate materials because of its high ionic conductivity [17], thermal conductivity [18], and sintering rate [19,20]; thus, many researchers have focused on new-generation T/EBC materials, such as $RE_2Si_2O_7$ (RE = rare earth) [8], RE_2SiO_5 [21], RE_3NbO_7 [22], $RE_2Zr_2O_7$ [23], $RE_2Ce_2O_7$ [24], and $RETaO_4$ [25].

Rare earth tantalates ($RETaO_4$, RE_3TaO_7, and $RETa_3O_9$) are considered novel E/TBCs because of their high melting point, ferroelastic ductility, moderate thermal expansion coefficient, low thermal/ionic conductivity, and high hardness (Table 1) [25–32]. However, the thermal conductivity of single rare earth tantalates is still high, and the ionic conductivity still needs to be reduced

✉ Corresponding authors.
E-mail: P. Wu, wu_peng@kust.edu.cn;
J. Feng, jingfeng@kmust.edu.cn

further [5,10]. To further improve the thermal insulating properties of rare-earth tantalates, in our previous work [31], five-component high-entropy $(Y_{1/5}Dy_{1/5}Sm_{1/5}Yb_{1/5}Er_{1/5})TaO_4$ exhibited a low thermal conductivity (1.21 $W{\cdot}m^{-1}{\cdot}K^{-1}$) (Table 1). To improve the thermal and oxygen barrier properties to a greater extent, here, we improve the crystal disorder of rare-earth tantalates by increasing the configurational entropy, which is responsible for enhancing the phonon and carrier scattering to reduce the thermal conductivity and oxygen ionic conductivity. Thus, high-entropy rare-earth tantalates ($(8RE_{1/8})TaO_4$) were designed and reassembled into a stabilized monoclinic structure to further decrease their thermal and ionic conductivity; moreover, even with high density, $(8RE_{1/8})TaO_4$ has low thermal conductivity and ensures high thermal insulation performance.

2 Experimental

2.1 Material design

The thermal conductivity is dominated by the phonon scattering coefficient (Γ), which is calculated on the basis of the ionic radius and atomic weights as Eq. (1) [33]:

$$\Gamma = f_i\left[\varepsilon\left(\frac{r_{i,s}-\overline{r}_s}{\overline{r}_s}\right)^2+\left(\frac{M_{i,s}-\overline{M}_s}{\overline{M}_s}\right)^2\right] \quad (1)$$

where f_i represents the content of the lattice defect; $r_{i,s}$ and $\overline{r}_s$ indicate the *i*-th-species ionic radius and the average ionic radius at the atomic site, respectively; $M_{i,s}$ and $\overline{M}_s$ indicate the *i*-th-species mass and the average mass at the atomic site, respectively. The size disorder and mass fluctuation as descriptors can predict the reduced thermal conductivity in high-entropy ceramics [34].

$$g_m = \sum\nolimits_{i=1}^{n} x_i\left(1-\frac{m_i}{\sum_{i=1}^{n}x_i m_i}\right)^2 \quad (2)$$

$$\delta_r = \sqrt{\sum\nolimits_{i=1}^{n} x_i\left(1-\frac{r_i}{\sum_{i=1}^{n}x_i r_i}\right)^2} \quad (3)$$

where x_i, m_i, and r_i is the atomic fraction, mass, and radius of the *i*-th component, respectively. High-entropy rare earth tantalates with large size disorder and mass disorder were obtained via calculations of different combinations. In addition, only one element change for each sample was used to obtain the effect of the element on its performance. For example, $(Y_{1/8}Dy_{1/8}Lu_{1/8}Yb_{1/8}Er_{1/8}Sm_{1/8}Nd_{1/8}Gd_{1/8})TaO_4$ (8HEC-1), $(Y_{1/8}Dy_{1/8}Lu_{1/8}Yb_{1/8}Er_{1/8}$-$Sm_{1/8}Nd_{1/8}Ho_{1/8})TaO_4$ (8HEC-2), and $(Y_{1/8}Dy_{1/8}Lu_{1/8}Yb_{1/8}Er_{1/8}Sm_{1/8}Nd_{1/8}Tm_{1/8})TaO_4$ (8HEC-3) are abbreviated as $(8RE_{1/8})TaO_4$. The effective RE^{3+} ionic radius (*r*, nm) [35] and relative atomic mass are listed in Table 2; the size disorder δ_r (%) and mass disorder g_m (%) related to the thermal conductivity are listed in Table 3.

2.2 Density functional theory calculations

Density functional theory (DFT) calculations were carried out employing the projected augmented wave (PAW) method as implemented in the Vienna *ab initio* simulation package (VASP). The electron exchange-correlation functional was given by Perdew–Burke–Ernzerhof (PBE) within the generalized gradient approximation (GGA). Equations (4) and (5) were used to determine the Gibbs free energy (*G*) [37]:

Table 1 Thermophysical properties of rare earth tantalates ($RETaO_4$, RE_3TaO_7, and $RETa_3O_9$), including Young's modulus (*E*, GPa), Grüneisen parameter (*γ*), Poisson's ratio (*ξ*), Debye temperature (θ_D, K), hardness (*H*, GPa), thermal conductivity (κ, $W{\cdot}m^{-1}{\cdot}K^{-1}$), thermal expansion coefficient (TEC, 10^{-6} K^{-1}), and oxygen ionic conductivity (*σ*, 10^{-6} $S{\cdot}cm^{-1}$)

Sample	*E*	*γ*	*ξ*	θ_D	*H*	κ	*TECs*	*σ*	Ref.
$YTaO_4$	138	2.13	0.35	354	5.1	1.74	9.6	7.7	[26,27] and this work
$NdTaO_4$	178	1.77	0.30	386	6.3	1.67	10.2	14.8	[25–27] and this work
$SmTaO_4$	171	1.80	0.30	373	—	1.35	10.2	13.9	[25–27] and this work
$GdTaO_4$	154	2.22	0.36	347	6.0	1.59	8.8	19.1	[25–27] and this work
$DyTaO_4$	135	1.97	0.33	352	5.2	1.82	9.9	—	[25–27] and this work
$ErTaO_4$	128	1.98	0.33	345	6.2	1.92	10.7	15.2	[25–27] and this work
Y_3TaO_7	240	1.71	0.29	447	—	1.31	9.2	—	[27]
Nd_3TaO_7	148	1.43	0.23	399	3.9	1.24	9.3	3.9	[27,29]
Sm_3TaO_7	212	1.59	0.27	406	—	4.50	6.1	—	[27]
Gd_3TaO_7	248	1.64	0.27	433	9.2	1.48	10.5	7.1	[27,29]
Dy_3TaO_7	250	1.66	0.28	466	10.2	1.61	10.2	5.6	[27,29]
$NdTa_3O_9$	190	1.47	0.24	392	9.1	1.96	5.7	—	[27,29]
$SmTa_3O_9$	185	1.51	0.25	402	9.2	1.58	5.7	—	[27,29]
$GdTa_3O_9$	192	1.61	0.24	400	9.3	1.40	3.5	—	[27,29]
$DyTa_3O_9$	190	1.60	0.26	423	8.8	1.56	9.9	—	[27,29]
$ErTa_3O_9$	194	1.62	0.27	411	9.2	1.55	6.3	—	[27,29]
$(Y_{1/5}Dy_{1/5}Sm_{1/5}Yb_{1/5}Er_{1/5})TaO_4$	117	1.83	0.33	326	4.2	1.21	9.01	—	[31]

Table 2 Effective RE^{3+} ionic radius (*r*, nm) [35] and relative atomic mass (*m*, g)

RE	Y	Nd	Sm	Gd	Dy	Ho	Er	Tm	Yb	Lu
r	0.1019	0.1109	0.1079	0.1053	0.1027	0.1015	0.1004	0.0994	0.0985	0.0977
m	88.906	144.24	150.36	157.25	162.50	164.93	167.26	166.93	173.05	174.97

Table 3 Size disorder δ_r (%) and mass disorder g_m (%) related to thermal conductivity

Sample	g_m (%)	δ_r (%)	Ref.
8HEC-1	2.901	4.168	This work
8HEC-2	2.933	4.136	This work
8HEC-3	2.950	4.272	This work
$(Nd_{1/4}Sm_{1/4}Eu_{1/4}Gd_{1/4})TaO_4$	0.094	1.928	[36]
$(Y_{1/5}Dy_{1/5}Sm_{1/5}Yb_{1/5}Er_{1/5})TaO_4$	4.273	3.083	[31]
$(Nd_{1/6}Sm_{1/6}Eu_{1/6}Gd_{1/6}Dy_{1/6}Ho_{1/6})TaO_4$	0.212	2.974	[36]

$$F(V,T) = E(V) + F_{ele}(V,T) + F_{vib}(V,T) \quad (4)$$

$$G = F(V,T) + PV \quad (5)$$

where $F(V,T)$ represents the Helmholtz free energy; $E(V)$ refers to the static energy at 0 K; P represents the atmospheric pressure. The Debye model (Eqs. (6) and (7)) was utilized to determine the vibrational contribution to the Gibbs free energy ($G = F$) when $P = 0$ [38,39]:

$$S = -\left(\frac{\partial F}{\partial T}\right)_V \quad (6)$$

$$H = F + TS \quad (7)$$

where H and S correspond to the entropy and enthalpy, respectively.

2.3 Material synthesis

The rare earth oxide powders RE_2O_3 (RE = Y, Dy, Lu, Yb, Er, Sm, Nd, Gd, Tm, and Ho) and tantalum oxide powders Ta_2O_5 were supplied by Shanghai Aladdin Bio-Chem Technology Co., Ltd., China. The raw materials were weighed according to the stoichiometric ratio and milled using a ZrO_2 ball with anhydrous ethanol as the medium at 300 r·min^{-1} for 10 h. The mixed powder was dried at 80 °C for 10 h and then sieved with a 500-mesh sieve. Subsequently, the mixed powder was placed into a graphite die (with an inner diameter of 15 mm), which was covered with thick graphite wool for thermal insulation. The die was placed on a spark plasma sintering (SPS) apparatus (SPS-632LX, Fuji Electronic Industrial Co., Ltd., Japan), and the sintering parameters are as follows: the axial pressure is 70 MPa; the maximum temperature is 1500 °C; the holding time at the highest temperature was 15 min; the heating ramp rate is 50 °C·min^{-1}. The samples were heat-treated to increase their density and eliminate the graphite component that migrated into the interior of the samples.

2.4 Microstructure characterization

An X-ray diffractometer (XRD; MiniFlex-600, Rigaku, Japan) and Fullprof software were used for Rietveld refinement of the crystal structure of samples. A powder high-temperature X-ray diffractometer (Panalytical, Empyrean, the Netherlands) was employed to investigate the high-temperature phase transitions of samples. The structure information was investigated by an X-ray photoelectron spectroscope (XPS; Thermo ESCALAB 250-type, Thermo Fisher Scientific, Waltham, USA) using standard monochromatic Al Kα radiation (1486.6 eV). The microstructures and ferroelastic domain structures of samples were observed by a scanning electron microscope (SEM; JSM-7001 F, JEOL, Japan) and a high-angle annual dark field-scanning transmission electron microscope (HAADF-STEM; ARM 200F, JEM, Japan). To reduce the scanning noise and sample drift during acquisition, atomic-resolution STEM and HAADF images were obtained by averaging a consecutive series of drift-corrected images. By carefully tuning the STEM machine, the size of the parallel probe used for nanobeam electron diffraction analysis was approximately 10 nm. The convergence angle was 0.18 mrad. In addition, the samples for TEM characterization were prepared by standard mechanical grinding and polished to a thickness of approximately 40 μm. Ar-ion thinning was performed via a precision ion milling system (model 691, Gatan Co., Ltd., Pleasanton, USA) with a gun voltage of 1.5–3.5 kV and a milling angle of 8°. After the sample was perforated, a voltage of 0.5 kV was used to optimize the thin area of the sample. The samples were further milled at a voltage of 0.1 kV to remove the damaged surface layer.

2.5 Thermo-mechanical property measurements

The thermal diffusivity (α) measurements were conducted in flowing argon gas with a laser flash instrument (LFA-427, NETZSCH, Germany) from room temperature to 1200 °C, and the thermal conductivity (κ) was calculated by Eq. (8) [40]:

$$\kappa = \alpha c_p \rho \quad (8)$$

The specific heat capacity c_p was calculated as the sum of the atomic heat capacities of the constituent oxides [41]. The density ρ was measured by the Archimedes method. The pores in the sample affect the thermal conductivity test; therefore, the actual thermal conductivity of the material was corrected as Eq. (9):

$$\kappa_0 = \kappa(1 - 4\varphi/3) \quad (9)$$

where κ_0 is the actual thermal conductivity; φ is the porosity of the sample ($\varphi = 1 - \rho/\rho_0$, where ρ_0 is the theoretical density of the sample obtained by Rietveld refinement of the crystal structure). The thermal expansion rates and thermal expansion coefficients (TECs) of the samples were measured using a thermomechanical analyzer (TMA-402 F3, NETZSCH, Germany).

Electrochemical impedance spectroscopy (EIS) was performed with an electrochemical workstation (SP-300, Bio-Logic, France) from 600 to 900 °C in a static ambient atmosphere over a frequency range of 0.01 Hz–2 MHz. At each test temperature ($\Delta T = 50$ °C), the samples were held for 30 min to achieve thermal equilibrium. Silver paste was printed on both surfaces of the ceramics and then sintered at 850 °C for 15 min as electrodes for EIS measurements. ZsimpWin software was employed to simulate the impedance spectra data. The electrical conductivities (σ) were calculated by Eq. (10):

$$\sigma = L/(R \cdot S) \quad (10)$$

where L is the sample thickness; S is the sample surface area; R is the total resistance. The activation energy was obtained by the Arrhenius law (Eq. (11)) [42]:

$$\sigma = (\sigma_0/T)\exp(-E_\alpha/(k_B T)) \quad (11)$$

where σ_0 is the pre-exponential factor; E_α is the activation energy; k_B is the Boltzmann constant; T is the thermodynamic temperature. The elastic properties were measured with a UMS Advanced Untrasonic Modulus measurement system (UMS-100, TECLAB, France) at room temperature. The Vickers hardness (H_V) was measured using the Vicker's indentation method (Buehler, Omnimet MHT, USA).

3 Results

3.1 Structural characterization

To predict the formation of a single-phase structure in high-entropy ceramics (HECs), density functional theory (DFT) was employed to calculate the Gibbs free energy, which is the determining factor in the phase stability of HECs; a higher entropy supports a lower Gibbs free energy and thus phase stability [43,44]. As shown in Fig. 1(a), $(8RE_{1/8})TaO_4$ has a negative Gibbs free energy in the range of 300–2000 K, and the results demonstrate that $(8RE_{1/8})TaO_4$ ceramics with a single-phase structure can be fabricated by a high-temperature solid-phase approach. However, the XRD results shown in Fig. 1(b) indicate the presence of a small amount of $RETa_3O_9$ in $Y_{1/8}Dy_{1/8}Lu_{1/8}Yb_{1/8}Er_{1/8}Sm_{1/8}Nd_{1/8}Ho_{1/8})TaO_4$ (8HEC-2) and $Y_{1/8}Dy_{1/8}Lu_{1/8}Yb_{1/8}$-$Er_{1/8}Sm_{1/8}Nd_{1/8}Tm_{1/8})TaO_4$ (8HEC-3), which may be the result of inhomogeneous ball milling. Figure 1(c) shows that the decreased average rare earth ion radius RE^{3+} ($r_{RE^{3+}} = 0.1032$ for 8HEC-1, $r_{RE^{3+}} = 0.1027$ for 8HEC-2 and $r_{RE^{3+}} = 0.1024$ for 8HEC-3) causes the XRD main peak (from 8HEC-1, to 8HEC-2, 8HEC-3) shift towards a higher diffraction angle. The *in-situ* XRD results shown in Fig. 1(d) demonstrate that the crystal structure $(Y_{1/8}Dy_{1/8}Lu_{1/8}Yb_{1/8}Er_{1/8}Sm_{1/8}Nd_{1/8}Tm_{1/8})TaO_4$ (8HEC-3) belongs to the m-phase at temperatures below 1500 °C, which is inconsistent with the conclusions reported by Qu *et al.* [45], who reported that $(Gd_{1-x}Y_x)TaO_4$ had a phase transition temperature of monoclinic (m) and tetragonal phase (t) from 1450 to 1500 °C, suggesting that the high-entropy 8HEC-3 has no phase transition and excellent phase stability below 1500 °C. Additionally, the XRD peak intensities at 2θ = 39.5° and 45.9° notably increase from 1400 to 1500 °C, suggesting a greater degree of crystallinity with increasing temperature. As shown in Figs. 1(e)–1(g), XRD refinement using Fullprof software was used to determine the distortion degree of $(8RE_{1/8})TaO_4$, and the crystal structure of $HoTaO_4$ (ICSD-79499) was used as the basis for refinement. The low goodness of fitting (GOF) of 1.32%–2.45% demonstrates the high accuracy of refined results, indicating that the $(8RE_{1/8})TaO_4$ solid solution maintains a monoclinic structure similar to that of $HoTaO_4$ (*C*2/*c*, No. 15). These findings indicate that the experimental XRD patterns agree well with the calculated data and Bragg positions.

Table 4 lists the lattice constants (*a*, *b*, and *c*), volume (*V*), and theoretical density (ρ_{cal}) obtained from Rietveld refinements. Table 5 lists the actual bond lengths of single-RE $RETaO_4$ [26] and $(8RE_{1/8})TaO_4$. There are three Ta–O and four RE–O bonds in $(8RE_{1/8})TaO_4$ since the TaO_4 and REO_8 polyhedrons are symmetric, while Chen et al. [26] reported only two Ta–O bond lengths in single-RE $RETaO_4$ since there were two sets of Ta–O with the same bond length. The bond length variation leads to distortion of TaO_4 and REO_8 polyhedrons, and the distortion degree of $(8RE_{1/8})TaO_4$ can be determined by Eq. (12) [46]:

$$\Delta d = \frac{1}{n}\sum_{i=1}^{n}\left[\frac{d(\mathrm{RE/Ta{-}O})_i - \overline{d(\mathrm{RE/Ta{-}O})}}{\overline{d(\mathrm{RE/Ta{-}O})}}\right]^2 \quad (12)$$

where $d(\mathrm{RE/Ta{-}O})_i$ and $\overline{d(\mathrm{RE/Ta{-}O})}$ represent the bond lengths of RE–O or Ta–O for the *i*-th O atom and their average bond length, respectively. Table 5 shows that the distortion degree Δd of TaO_4 is significantly higher than that of REO_8 in

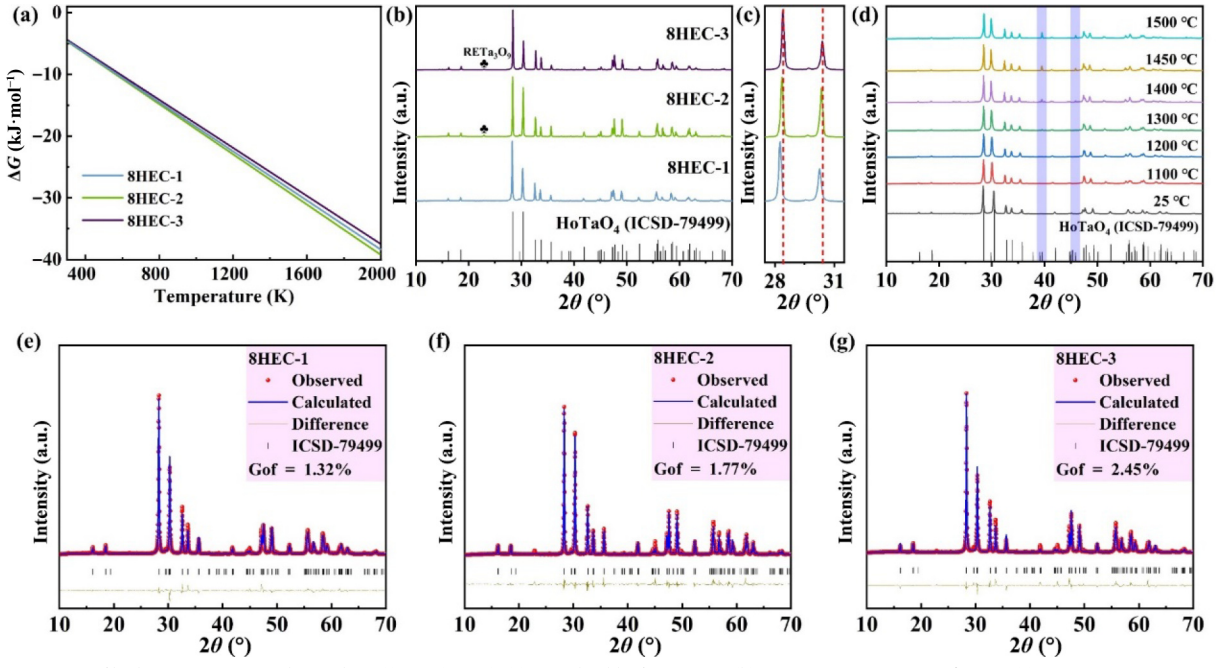

Fig. 1 Structure of high-entropy rare-earth tantalates ($(8RE_{1/8})TaO_4$): (a) mixed Gibbs free energy; (b) XRD patterns at 10° ≤ 2θ ≤ 70°; (c) XRD patterns at 27.5° ≤ 2θ ≤ 31.5°; (d) *in-situ* XRD patterns; (e–g) Rietveld refinement of XRD patterns.

Table 4 Lattice constants (*a*, *b*, *c*; Å), β (°), volume (*V*, Å^3) and theoretical density (ρ_{cal}, g·cm^{-3}) of $(8RE_{1/8})TaO_4$ obtained from Rietveld refinements

Parameter	*a*	*b*	*c*	β	*V*	ρ_{cal}
8HEC-1	5.35735	10.9885	5.06565	95.5509	296.813	8.890
8HEC-2	5.34960	10.9738	5.06290	95.5446	295.830	8.941
8HEC-3	5.34578	10.9694	5.06001	95.5342	295.336	8.967

$(8RE_{1/8})TaO_4$ ceramics, and the total distortion degree Δd_{tot} in $(8RE_{1/8})TaO_4$ ceramics is higher than that in single-RE $RETaO_4$ ceramics, indicating that the high entropy effect induces severe lattice distortion. Moreover, the Δd_{tot} of $(8RE_{1/8})TaO_4$ ceramics is also greater than that of $(Y_{1/5}Dy_{1/5}Sm_{1/5}Yb_{1/5}Er_{1/5})TaO_4$ ceramics [31], suggesting that the increase in conformational entropy contributes to the increase in lattice distortion. Comparing Figs. 1(e) and 1(f), the $RETa_3O_9$ peak intensity of $(Y_{1/8}Dy_{1/8}Lu_{1/8}Yb_{1/8}Er_{1/8}Sm_{1/8}Nd_{1/8}Ho_{1/8})$–$TaO_4$ (8HEC-2) at 23° is significantly higher than that of $(Y_{1/8}Dy_{1/8}Lu_{1/8}Yb_{1/8}Er_{1/8}$–$Sm_{1/8}Nd_{1/8}Gd_{1/8})TaO_4$ (8HEC-1) and $(Y_{1/8}Dy_{1/8}Lu_{1/8}$–$Yb_{1/8}Er_{1/8}Sm_{1/8}Nd_{1/8}Tm_{1/8})TaO_4$ (8HEC-3), suggesting that 8HEC-2 has a higher $RETa_3O_9$ content, which may lead to the higher lattice distortion in 8HEC-2.

The XPS survey spectra in Fig. 2(a) show the presence of Ta, O, and RE elements in $(8RE_{1/8})TaO_4$. Figure 2(b) shows the XPS high-resolution spectra of the Ta 4f region, the Ta 4f peak appears as a doublet due to the spin–orbit splitting with a value of 1.87 eV for $(Y_{1/8}Dy_{1/8}Lu_{1/8}Yb_{1/8}Er_{1/8}Sm_{1/8}Nd_{1/8}Gd_{1/8})TaO_4$ (8HEC-1), 1.89 eV for $(Y_{1/8}Dy_{1/8}Lu_{1/8}Yb_{1/8}Er_{1/8}Sm_{1/8}Nd_{1/8}Ho_{1/8})TaO_4$ (8HEC-2), and 1.85 eV for $(Y_{1/8}Dy_{1/8}Lu_{1/8}Yb_{1/8}Er_{1/8}Sm_{1/8}Nd_{1/8}Tm_{1/8})TaO_4$ (8HEC-3). The spin-orbit splitting component of the fitting spectra has a ratio of 3 : 4, revealing only one chemical state of Ta^{5+}, which is in good agreement with Refs. [47,48]. To analyze the oxygen vacancies in connection with the thermal and ionic conductivity of $(8RE_{1/8})TaO_4$ ceramics, XPS was used to identify their oxygen vacancies. Figure 2(c) and Table S1 in the Electronic Supplementary Material (ESM) display the binding energies of O 1s at 530.01–530.05 and 532.81–532.87 eV, corresponding to the peaks of lattice oxygen (O_{lat}) and physically adsorbed oxygen (O_{ads}), respectively [49], and the peak of O 1s at intermediate binding energies (531.41–531.73 eV) is typically attributed to oxygen vacancies ($V_{\ddot{O}}$), which is consistent with Refs. [50–52].

3.2 Microstructure and ferroelastic domain structures

Figures 3(a)–3(g) show SEM images of $(Y_{1/8}Dy_{1/8}Lu_{1/8}Yb_{1/8}Er_{1/8}Sm_{1/8}Nd_{1/8}$–$Tm_{1/8})TaO_4$ (8HEC-3) at different heat treatment temperatures, and the results reveal that the grain size and relative density increase as the heat treatment temperature increases. The nanograin sizes in Figs. 3(a) and 3(b) are too small to be counted because of the low heat treatment temperature. Figure 3(h) shows that the average grain size increases from 0.15 μm at 1200 °C to 9.62 μm at 1600 °C, and the porosity

Table 5 Bond length (Ta–O and RE–O) and distortion degree (Δd, %) of $(8RE_{1/8})TaO_4$, single-RE $RETaO_4$ [26], and $(Y_{1/5}Dy_{1/5}Sm_{1/5}Yb_{1/5}Er_{1/5})TaO_4$ [31]

Sample	Bond	Bond length (l, Å)				$\bar{l}$	Δd (%)	Δd_{tot} (%)
8HEC-1	Ta–O	1.82918	1.97271	2.36377	—	2.0552	1.2082	1.2467
	RE–O	2.32057	2.33318	2.3914	2.43637	2.3704	0.0385	
8HEC-2	Ta–O	1.80923	1.95007	2.54339	—	2.1009	2.2930	2.7861
	RE–O	2.06216	2.3999	2.43151	2.47842	2.3430	0.4931	
8HEC-3	Ta–O	1.81683	1.97555	2.36982	—	2.0541	1.2810	1.3104
	RE–O	2.31721	2.38862	2.38821	2.43091	2.3812	0.0294	
$(Y_{1/5}Dy_{1/5}Sm_{1/5}Yb_{1/5}Er_{1/5})TaO_4$	Ta–O	1.8519	1.9361	2.3240	—	2.0373	1.0183	1.0700
	RE–O	2.2927	2.3295	2.3538	2.4382	2.3536	0.0517	
$YTaO_4$	Ta–O	2.0646	1.9377	—	—	2.0011	0.1005	0.1332
	Y–O	2.3352	2.3049	2.2688	2.2245	2.2833	0.0327	
$NdTaO_4$	Ta–O	1.9773	1.7866	—	—	1.8819	0.2566	0.3192
	Nd–O	2.5722	2.5099	2.4568	2.4046	2.4858	0.0626	
$SmTaO_4$	Ta–O	2.0052	1.9281	—	—	1.9666	0.0384	0.3884
	Sm–O	2.5355	2.4919	2.3088	2.1859	2.3805	0.3500	
$GdTaO_4$	Ta–O	1.9130	1.8256	—	—	1.8693	0.0546	0.2224
	Gd–O	2.5283	2.5089	2.3457	2.3009	2.4209	0.1678	
$DyTaO_4$	Ta–O	1.9400	1.8173	—	—	1.9249	0.1066	0.2694
	Dy–O	2.4257	2.4172	2.3361	2.1902	2.3423	0.1628	
$HoTaO_4$	Ta–O	1.9326	1.9317	—	—	1.9321	0	0.1250
	Ho–O	2.3881	2.3626	2.3660	2.3157	2.3581	0.1250	
$ErTaO_4$	Ta–O	2.0074	1.8425	—	—	1.9249	0.1834	0.3600
	Er–O	2.5443	2.4575	2.3935	2.2659	2.4153	0.1766	

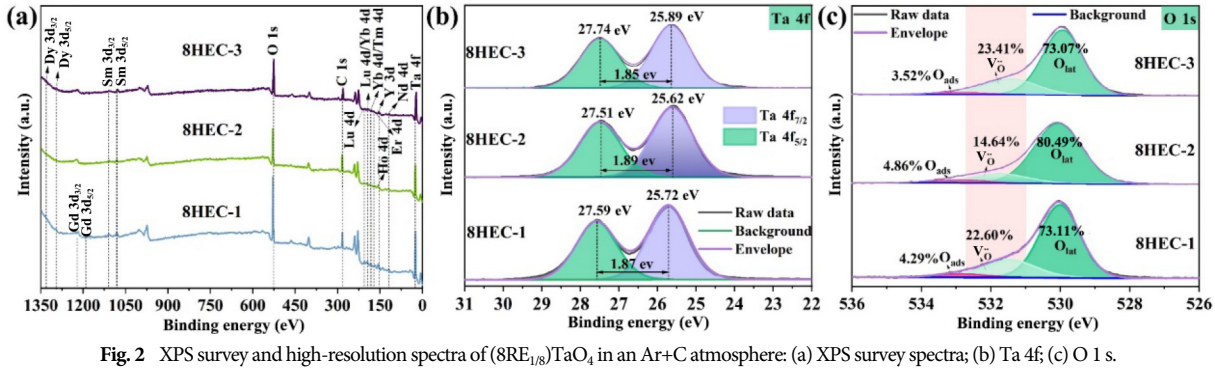

Fig. 2 XPS survey and high-resolution spectra of $(8RE_{1/8})TaO_4$ in an Ar+C atmosphere: (a) XPS survey spectra; (b) Ta 4f; (c) O 1 s.

清華大学出版社 Tsinghua University Press | SciOpen

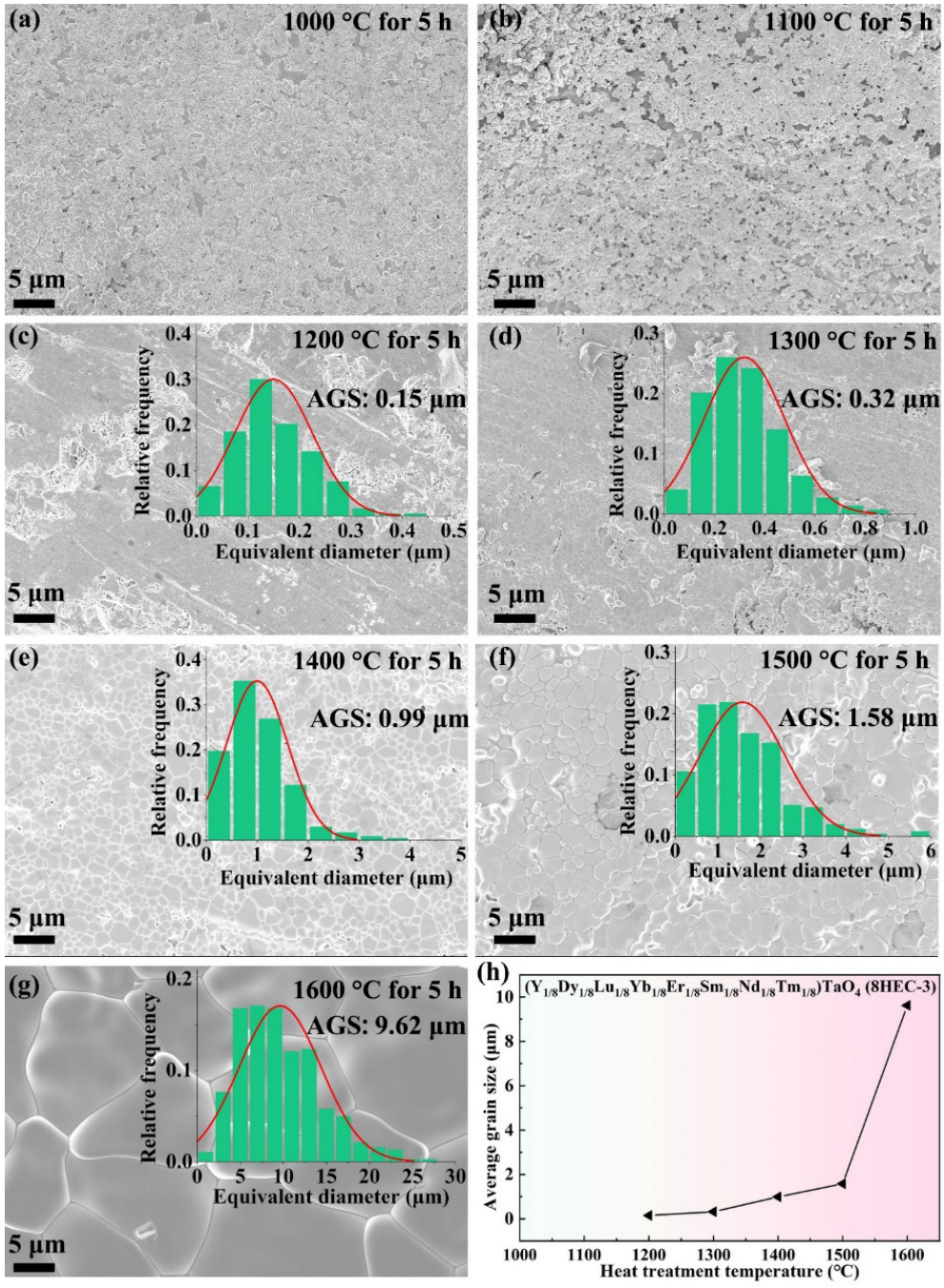

Fig. 3 SEM images and average grain size of 8HEC-3 at various heat treatment temperatures.

increases from 93% at 1000 °C to 97.5% at 1600 °C. To achieve more dense samples, $(Y_{1/8}Dy_{1/8}Lu_{1/8}Yb_{1/8}Er_{1/8}Sm_{1/8}Nd_{1/8}Gd_{1/8})TaO_4$ (8HEC-1), $(Y_{1/8}Dy_{1/8}Lu_{1/8}Yb_{1/8}Er_{1/8}$–$Sm_{1/8}Nd_{1/8}Ho_{1/8})TaO_4$ (8HEC-2), and $(Y_{1/8}Dy_{1/8}Lu_{1/8}Yb_{1/8}$–$Er_{1/8}Sm_{1/8}Nd_{1/8}Tm_{1/8})TaO_4$ (8HEC-3) were heat-treated at 1600 °C for 5 h.

Figures 4(a)–4(c) show the SEM images of $(8RE_{1/8})TaO_4$ ceramics after heat treatment at 1600 °C for 5 h. The distribution of grains with various shapes at the grain boundaries of $(Y_{1/8}Dy_{1/8}Lu_{1/8}Yb_{1/8}Er_{1/8}Sm_{1/8}Nd_{1/8}Ho_{1/8})TaO_4$ (8HEC-2) may be a result of melt overflow from the grain boundaries during grain growth, which contributes to the improvement in ceramic density. In addition, the three samples have a similar average grain size (AGS) of 10.06 μm for $(Y_{1/8}Dy_{1/8}Lu_{1/8}Yb_{1/8}Er_{1/8}Sm_{1/8}Nd_{1/8}Gd_{1/8})TaO_4$ (8HEC-1), 11.31 μm for $(Y_{1/8}Dy_{1/8}Lu_{1/8}Yb_{1/8}Er_{1/8}Sm_{1/8}Nd_{1/8}Ho_{1/8})TaO_4$ (8HEC-2), and 9.62 μm for $(Y_{1/8}Dy_{1/8}Lu_{1/8}Yb_{1/8}Er_{1/8}Sm_{1/8}Nd_{1/8}Tm_{1/8})TaO_4$ (8HEC-3). Therefore, the effects of grain size on the thermal conductivity and oxygen ion conductivity can be considered similar for all three samples. The enlarged SEM images in Figs. 4(d)–4(f) show that diverse grains have parallel fringe structures in different directions, which are considered ferroelastic domain structures [53,54]. The domain structure results from the volume difference created by the reversible secondary phase transition T ⟷ M, where the high-temperature tetragonal (T) phase only exists in a high-temperature environment, the monoclinic phase (M) can be retained at room temperature [55], and the temperature of the secondary phase transition (T ⟷ M) is approximately 1426±7 °C [56,57]. The EDS results in Fig. 5 indicate that the composition of $(8RE_{1/8})TaO_4$ ceramics is uniformly distributed without significant segregation or aggregation.

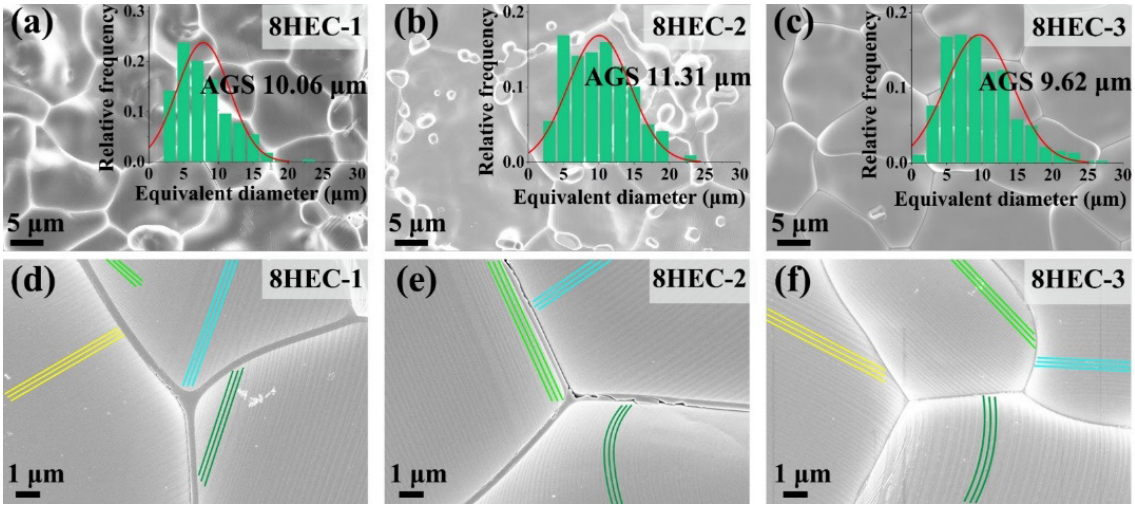

Fig. 4 Microstructure and grain size distribution of $(8RE_{1/8})TaO_4$: (a–c) SEM images and grain size distribution; (d–f) magnified SEM images with a domain structure.

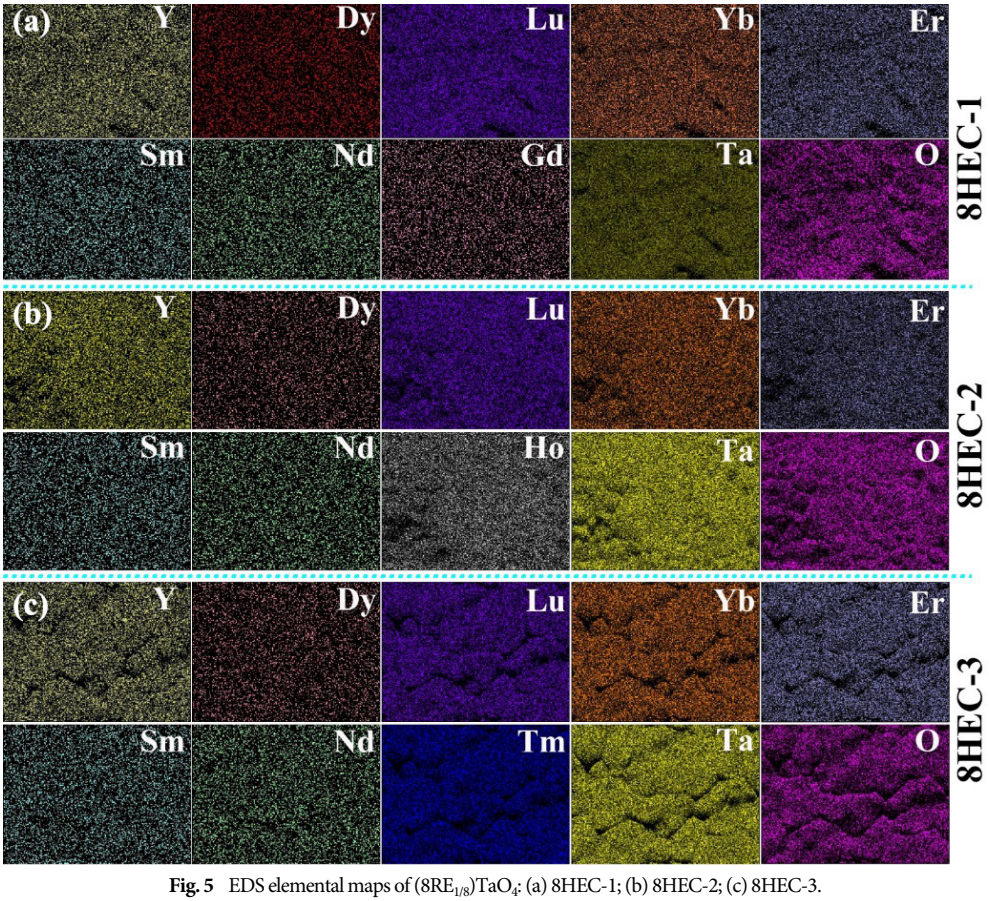

Fig. 5 EDS elemental maps of $(8RE_{1/8})TaO_4$: (a) 8HEC-1; (b) 8HEC-2; (c) 8HEC-3.

3.3 Thermal properties

The selection of T/EBC materials that match the thermal expansion coefficients (TECs) of the bonded coating is another important indicator of long service life [58]. The thermal expansion coefficients (TECs) of multicomponent high-entropy rare-earth tantalate $(8RE_{1/8})TaO_4$ were investigated to further verify its viability as a T/EBC material. As shown in Fig. 6(a), the TECs of 8HEC-1 and 8HEC-2 are comparable and lower than that of 8HEC-3 (11.5×10^{-6} K^{-1}@1200 °C). The thermal expansion coefficient of ionic crystals can be associated with the ionic bond strength I_{A-B} [59], which is closely related to the electronegativity difference $x_A - x_B$ based on Eq. (13) [60,61].

$$I_{A-B} = 1 - e^{-\frac{x_A - x_B}{4}} \quad (13)$$

where x is the average electronegativity and the subscripts A and B are cations and anions, respectively. Equation (13) shows that a high thermal expansion coefficient always corresponds to a low value of $x_A - x_B$. For $(Y_{1/8}Dy_{1/8}Lu_{1/8}Yb_{1/8}Er_{1/8}Sm_{1/8}Nd_{1/8}Gd_{1/8})TaO_4$ (8HEC-1), $(Y_{1/8}Dy_{1/8}Lu_{1/8}Yb_{1/8}Er_{1/8}$–$Sm_{1/8}Nd_{1/8}Ho_{1/8})TaO_4$ (8HEC-2), and $(Y_{1/8}Dy_{1/8}Lu_{1/8}Yb_{1/8}Er_{1/8}Sm_{1/8}Nd_{1/8}Tm_{1/8})TaO_4$ (8HEC-3) ceramics, RE^{3+} and Ta^{5+} occupy A sites, and only O^{2-} occupies B sites in A_mB_n ion crystals. The average electrical negativities of RE^{3+} and Ta^{5+} at A sites are 1.3475 for 8HEC-1, 1.349375 for 8HEC-2, and 1.350625 for 8HEC-3; the electrical negativities of O^{2-} are 3.44; and the ionic bond I_{A-B} values are

0.6653 for 8HEC-1, 0.6647 for 8HEC-2, and 0.6642 for 8HEC-3. Therefore, 8HEC-3 has a higher thermal expansion coefficient because of its low ionic bond strength.

As shown in Fig. 6(b), the experimental thermal diffusivities (α_{exp}) of single-RE $RETaO_4$ and $(8RE_{1/8})TaO_4$ decrease as the temperature rises due to the gradual increase in phonon scattering. However, the experimental thermal diffusivity unexpectedly increases as the temperature increases further because of enhanced radiative transfer [62,63]. Compared with single-RE $RETaO_4$, $(8RE_{1/8})TaO_4$ exhibits much lower experimental thermal diffusivity. Figure 6(c) shows that the experimental thermal conductivity (κ_{exp}) of $(8RE_{1/8})TaO_4$ is lower than those of 8YSZ, $(Y_{1/5}Dy_{1/5}Sm_{1/5}Yb_{1/5}Er_{1/5})TaO_4$ [31], and most single-RE tantalates, indicating that high-entropy ceramics $(8RE_{1/8})TaO_4$ with high conformational entropy have excellent thermal insulation for the thermal protection of substrate.

3.4 Oxygen barrier properties

The typical AC impedance plots of single-RE $RETaO_4$, $(8RE_{1/8})TaO_4$, and 8YSZ ceramics at 650–900 °C are shown in Figs. S1 and S2 in the ESM. As shown in Fig. 7, the oxygen ion conductivities of single-RE $RETaO_4$, $(8RE_{1/8})TaO_4$ and 8YSZ increase with increasing temperature. At high temperatures, the number of carriers from the valence band excitation to the conduction band increases, and the deviation of atoms from the ideal position leads to an increase in oxygen vacancy concentration; that is, more carriers participate in conduction; thus, the resistivity decreases, and the conductivity increases. As is evident from Fig. 7 and Table S2 in the ESM, the oxygen ion conductivities (σ) of 8YSZ, single-RE $RETaO_4$ and $(8RE_{1/8})TaO_4$ in descending order is σ(8YSZ) > $\sigma(HoTaO_4)$ > $\sigma(TmTaO_4)$ > $\sigma(GdTaO_4)$ > $\sigma(YbTaO_4)$ > $\sigma(ErTaO_4)$ > $\sigma(NdTaO_4)$ > $\sigma(SmTaO_4)$ > $\sigma(LuTaO_4)$ > $\sigma(YTaO_4)$ > $\sigma(Y_{1/8}Dy_{1/8}Lu_{1/8}Yb_{1/8}Er_{1/8}Sm_{1/8}Nd_{1/8}$–$Ho_{1/8})TaO_4$ (8HEC-2) > $\sigma(Y_{1/8}Dy_{1/8}Lu_{1/8}Yb_{1/8}Er_{1/8}Sm_{1/8}Nd_{1/8}Gd_{1/8})TaO_4$ (8HEC-1) > $\sigma(Y_{1/8}Dy_{1/8}Lu_{1/8}Yb_{1/8}Er_{1/8}Sm_{1/8}Nd_{1/8}Tm_{1/8})TaO_4$ (8HEC-3). Compared with that of 8YSZ, the oxygen ion conductivity of $(8RE_{1/8})TaO_4$ decreases by 3–5 orders of magnitude in the range from 600 to 900 °C, and the oxygen ion conductivity of $8(RE_{1/8})TaO_4$ is further decreased by the high entropy effect compared with that of single-RE $RETaO_4$.

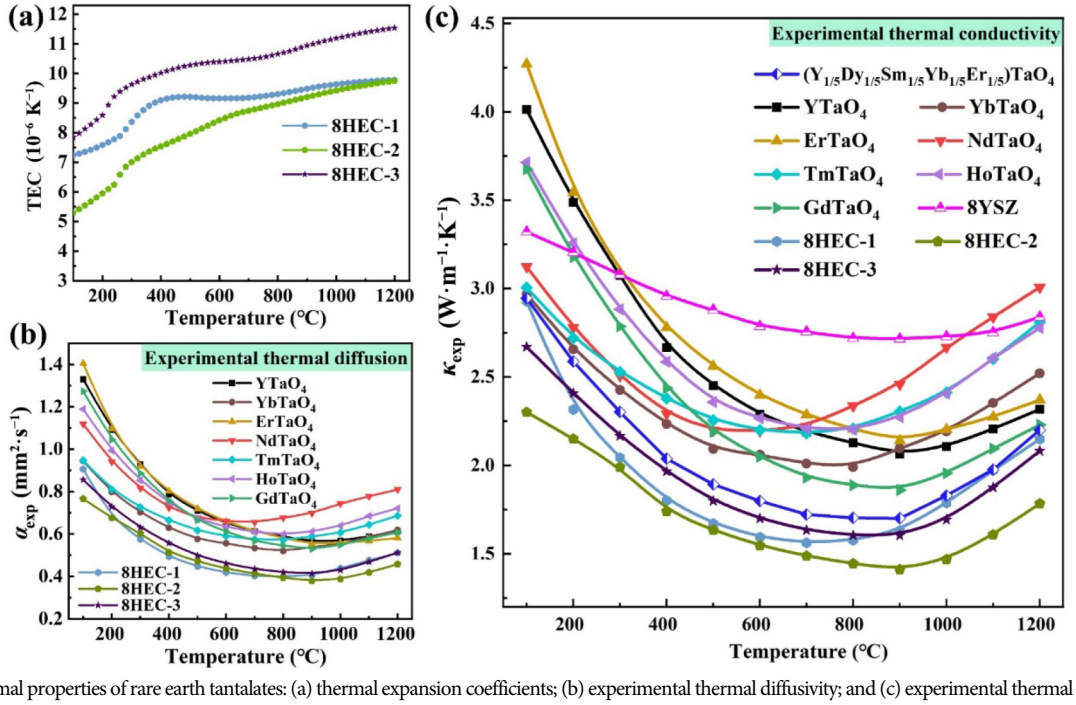

Fig. 6 Thermal properties of rare earth tantalates: (a) thermal expansion coefficients; (b) experimental thermal diffusivity; and (c) experimental thermal conductivity.

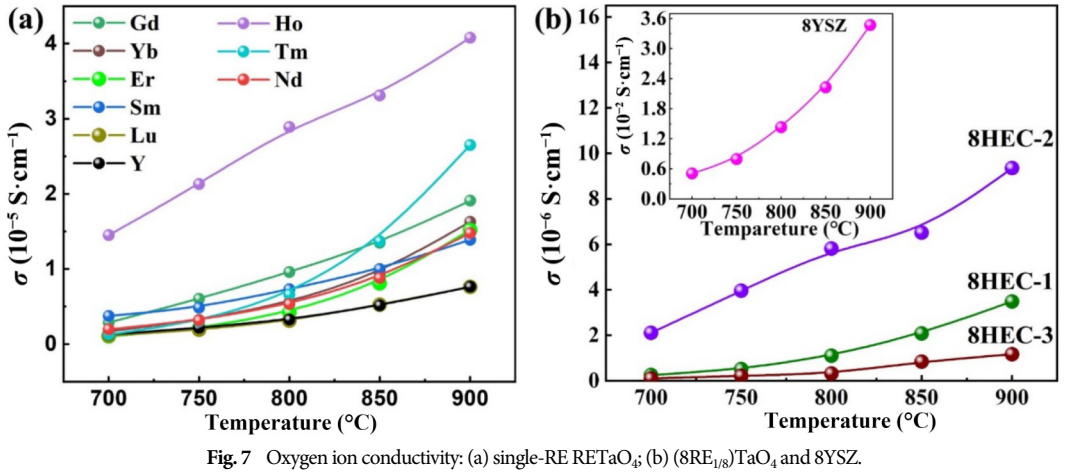

Fig. 7 Oxygen ion conductivity: (a) single-RE $RETaO_4$; (b) $(8RE_{1/8})TaO_4$ and 8YSZ.

3.5 Mechanical properties

The ultrasonic pulser method was employed to measure the elastic properties of $(8RE_{1/8})TaO_4$. Through the transverse acoustic velocity (v_t) and longitudinal acoustic velocity (v_l), the average acoustic velocity (v_m), Poisson's ratio (ξ), Young's modulus (E), bulk modulus (B), and shear modulus (G) are calculated by Eqs. (14)–(20) [64]:

$$v_m = \left[\frac{1}{3}\left(\frac{1}{v_l^3} + \frac{2}{v_t^3}\right)\right]^{-\frac{1}{3}} \tag{14}$$

$$\zeta = \frac{1 - 2(v_t/v_l)^2}{2 - 2(v_t/v_l)^2} \tag{15}$$

$$E = \frac{\rho v_t^2(3v_l^2 - 4v_t^2)}{(v_l^2 - v_t^2)} \tag{16}$$

$$G = \frac{E}{2(2+\sigma)} \tag{17}$$

$$B = \rho\left(v_l{}^2 - \frac{4}{3}v_t{}^2\right) \tag{18}$$

$$\gamma = \frac{3}{2}\left(\frac{1+\sigma}{2-3\sigma}\right) \tag{19}$$

$$\theta_D = \frac{h}{k_B}\left(\frac{3N}{4\pi V}\right)^{\frac{1}{3}} \times v_m \tag{20}$$

where h, k_B, N, V, γ, and θ_D are Plank's constant, the Boltzmann constant, the number of atoms in a unit cell, the volume of the unit cell, the Grüneisen parameter, and the Debye temperature, respectively. As shown in Table 6, compared with five-component $(Y_{1/5}Dy_{1/5}Sm_{1/5}Yb_{1/5}Er_{1/5})TaO_4$ [31], $(Y_{1/8}Dy_{1/8}Lu_{1/8}Yb_{1/8}Er_{1/8}–Sm_{1/8}Nd_{1/8}Gd_{1/8})TaO_4$ (8HEC-1), $(Y_{1/8}Dy_{1/8}Lu_{1/8}Yb_{1/8}Er_{1/8}Sm_{1/8}Nd_{1/8}Ho_{1/8})TaO_4$ (8HEC-2), and $(Y_{1/8}Dy_{1/8}Lu_{1/8}Yb_{1/8}Er_{1/8}Sm_{1/8}Nd_{1/8}Tm_{1/8})TaO_4$ (8HEC-3) have lower Young's moduli. In addition, the ratio of the bulk modulus to the shear modulus (G/B) can be used to evaluate the ductility of a material; brittle materials have a G/B ratio below 0.57; otherwise, they are ductile materials [65]. The G/B ratios of 8HEC-1, 8HEC-2, 8HEC-3, and $(Y_{1/5}Dy_{1/5}Sm_{1/5}Yb_{1/5}Er_{1/5})TaO_4$ [31] are 0.55, 0.54, 0.51, and 0.38, respectively, indicating that these high-entropy rare-earth tantalates are brittle materials. Hardness is an important descriptor of the resistance of thermal barrier coating materials to permanent localized deformation [66]. The hardnesses tested by the indentation method in Fig. 8 are 5.9 GPa for 8HEC-1, 6.3 GPa for 8HEC-2, and 5.1 GPa for 8HEC-3 when the load is 9.8 N, which exceed that of $(Y_{1/5}Dy_{1/5}Sm_{1/5}Yb_{1/5}Er_{1/5})TaO_4$ (4.2 GPa) [31] but is inferior to that of 8YSZ (13–14.2 GPa) [67]. Additionally, there is a significant amount of crack propagation rather than radial cracks within the three samples, so the fracture toughness cannot be calculated. The crack propagation around the indentation apex efficiently alleviates the stress concentration and diminishes the fracture energy, hence increasing the toughness.

4 Discussion

4.1 Domain switching and oxygen vacancy formation mechanisms

The ferroelastic domain structures are shown in Fig. 9. The needle-like structures are domain structures in Fig. 9(a), and the average widths of the domain region and needle-like domain walls are 95.4 and 21.2 nm, respectively. Figure S3 in the ESM shows that the mean free path of phonons at 100–1200 °C is 0.38–1.04 nm, and the width of the domain wall is closer to the mean free path of phonons. The atomic configurations depicted in Fig. 9(b) can be divided into two monoclinic phase variants, i.e., M_1 phase and M_2 phase, with the main difference between the two being the distance between the atomic planes. For the M_1 variant along [001] zone axis, the distance between adjacent Ta atomic columns ($d_{Ta–Ta}$) is 0.337 nm, and the distance between the adjacent Ta atomic column and the Y atomic column ($d_{Ta–Y}$) is 0.273 nm. However, for the M_2 variant, $d_{Ta–Ta}$ and $d_{Ta–Y}$ are 0.289 and 0.305 nm, respectively, indicating that the distances between adjacent atomic columns on both sides of the domain boundary are different. The SAED pattern in Fig. 9(c) further proves that the domain structure is formed by changing the distance between atomic planes. The needle-like domain structures prove that the variant could switch from one to another. Wang *et al.* [53] reported that the domain walls formed near the atomic deflection at the $[2\bar{1}2]$ zone axis, and the SAED patterns at areas M_1 and M_2 needed to be rotated at a certain angle to overlap completely, indicating that there are different domain configurations along

Table 6 Mean acoustic velocity (v_m, m·s^{-1}), Young's modulus (E, GPa), bulk modulus (B, GPa), shear modulus (G, GPa), Grüneisen parameter (γ), Poisson's ratio (ξ), and Debye temperature (θ_D, K)

Sample	v_m	E	B	G	γ	ξ	θ_D
8HEC-1	1981	60	44	24	1.60	0.27	257
8HEC-2	2232	89	68	35	1.66	0.28	287
8HEC-3	2242	91	69	35	1.65	0.28	290
$(Y_{1/5}Dy_{1/5}Sm_{1/5}Yb_{1/5}Er_{1/5})TaO_4$ [31]	2531	117	117	44	2.00	0.33	326

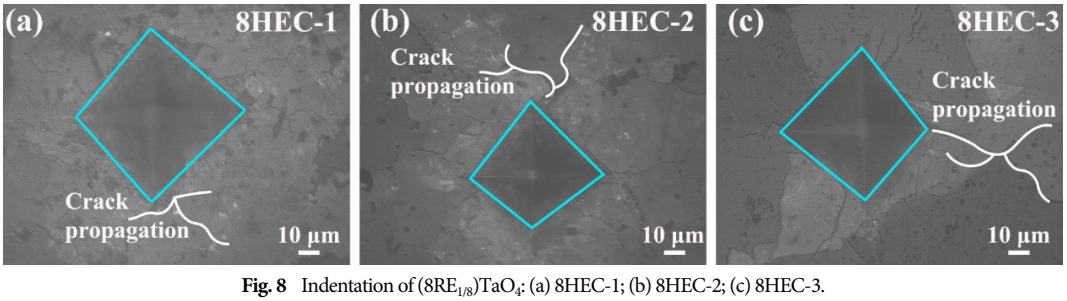

Fig. 8 Indentation of $(8RE_{1/8})TaO_4$: (a) 8HEC-1; (b) 8HEC-2; (c) 8HEC-3.

different zone axes. In addition, introducing dislocations at grain boundaries has the potential to decrease the thermal conductivity and ionic conductivity. Kim *et al.* [68] reported that the dense dislocation arrays within grain boundaries had a limited impact on the scattering of charge carriers; however, these dislocation arrays exhibited a remarkable ability to scatter phonons, resulting in a significant reduction in thermal conductivity. Figure 9(a) shows the dislocation lines of $(Y_{1/8}Dy_{1/8}Lu_{1/8}Yb_{1/8}Er_{1/8}Sm_{1/8}Nd_{1/8}Tm_{1/8})TaO_4$ (8HEC-3); the dislocation arrays may cause complex strain distributions and target mid-frequency phonon scattering, leading to a significant reduction in the lattice thermal conductivity [68].

Oxygen vacancies are formed because Ta_2O_5 has a greater saturated vapor pressure than RE_2O_3 [69–71]; some Ta_2O_5 volatilizes prior to reacting with RE_2O_3 at high temperatures, which reflects the inverse relationship between vapor pressure and rate of volatilization. Furthermore, we demonstrate that Ta_2O_5 volatilizes at a greater rate than RE_2O_3 via high-temperature experiments, as shown in Table S3 in the ESM. In parallel, the mass of bulk material $(8RE_{1/8})TaO_4$ decreases after calcination at 1700 °C for 5 h, indicating that the volatilization of raw materials results in a deviation of $(8RE_{1/8})TaO_4$ composition from the stoichiometric ratio. Figure 10 shows that each tantalum atom occupies its own lattice site, but rare earth atoms fill both the rare earth atom lattice and the tantalum atom lattice site, leading to the formation of oxygen vacancies based on Kröger–Vink notation (Eq. (21)) [72]:

$$RE_2O_3 \xrightarrow{RETaO_4} RE_{RE}^{\times} + RE_{Ta}^{''} + 3O_O^{\times} + V_O^{\cdot\cdot} \quad (21)$$

where the symbol $RE_{RE}^{\times}$ denotes RE^{3+} ions occupying the RE^{3+} cation site with a neutral charge. Similarly, $RE_{Ta}^{''}$ represents RE^{3+} ions occupying the Ta^{5+} cation site with a doubly negative charge. The symbol $O_O^{\times}$ indicates an oxygen vacancy with a doubly positive charge.

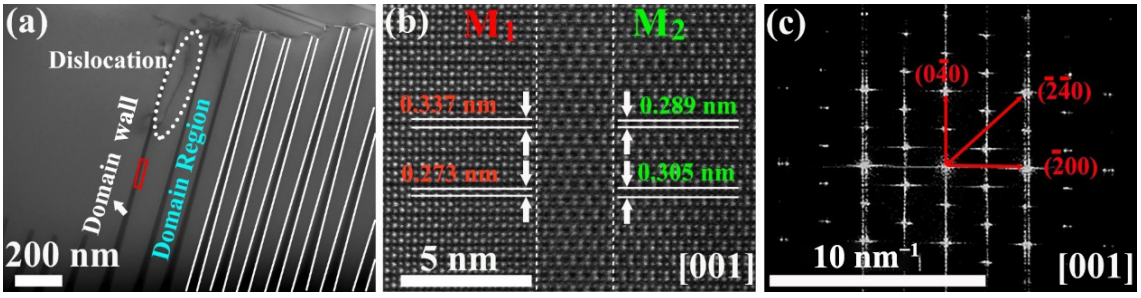

Fig. 9 STEM-HAADF image of 8HEC-3: (a) dislocation and ferroelastic domain structures; (b) magnified STEM-HAADF image of the red rectangular box in (a); (c) SAED patterns corresponding to (b).

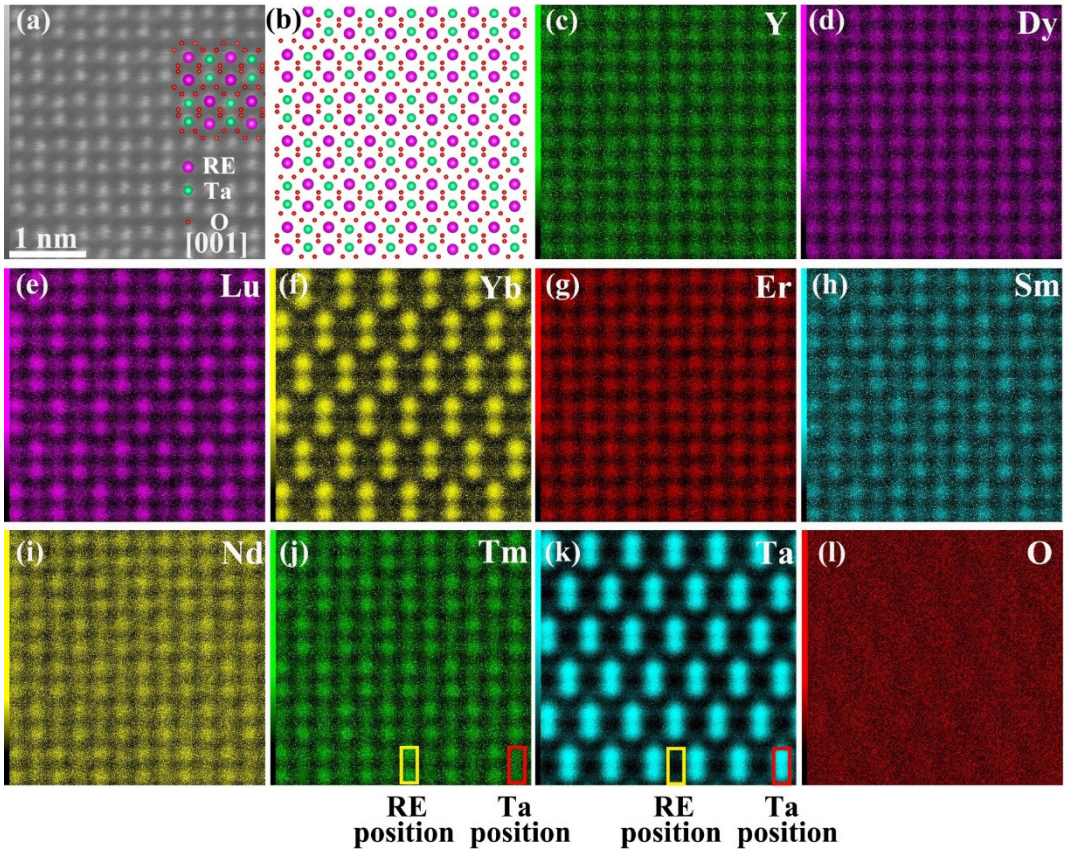

Fig. 10 STEM-EDS analysis of 8HEC-3: (a) HAADF image along [001] zone axis; (b) schematic diagram of atomic structure oriented along [001] zone axis. (c–l) Intensity maps correspond to Y, Dy, Lu, Yb, Er, Sm, Nd, Tm, Ta, and O atoms, respectively.

4.2 Mechanism of ultra-low thermal conductivity

Figure 11(a) shows that the reciprocal of experimental thermal diffusivity (α_{exp}^{-1}) no longer follows a linear relationship and instead steadily decreases at temperatures above 500 °C, indicating that $(8RE_{1/8})TaO_4$ has a high thermal-radiation conductivity. The intrinsic thermal diffusivity in the absence of thermal radiation effects was calculated using Eq. (22) [73]:

$$\frac{1}{\alpha}\infty\frac{1}{l(w,T)}\infty\left(\frac{bn^{1/3}C}{\theta_D}\right)T+\left(D-\frac{C}{2}\right) \quad (22)$$

where $l(w,T)$ denotes the phonon mean free path; T is the absolute temperature; n denotes the number of atoms in the primitive cell; C and D denote proportionality constants; b is approximately equal to 2; and θ_D is the Debye temperature. The reciprocal of intrinsic thermal diffusivity (α_{int}^{-1}) is fitted in Fig. 11(a). For example, the fitting equation is as follows: $\alpha_{int}^{-1}=0.00282T+0.87278$ for $(Y_{1/8}Dy_{1/8}Lu_{1/8}Yb_{1/8}Er_{1/8}$–$Sm_{1/8}Nd_{1/8}Gd_{1/8})TaO_4$ (8HEC-1), $\alpha_{int}^{-1}=0.00204T+1.08698$ for $(Y_{1/8}Dy_{1/8}Lu_{1/8}Yb_{1/8}$-$Er_{1/8}Sm_{1/8}Nd_{1/8}Ho_{1/8})TaO_4$ (8HEC-2), and $\alpha_{int}^{-1}=0.00203T+0.97134$ for $(Y_{1/8}Dy_{1/8}$-$Lu_{1/8}Yb_{1/8}Er_{1/8}Sm_{1/8}Nd_{1/8}Tm_{1/8})TaO_4$ (8HEC-3). Furthermore, Fig. S4 in the ESM shows the intrinsic thermal diffusion (α_{int}) calculated by above linear fitting equation, and the intrinsic thermal conductivity (κ_{int}) was determined by α_{int}. As shown in Fig. 11(b), compared with 8YSZ, the κ_{int} of $(8RE_{1/8})TaO_4$ is reduced by 59.2%–67.5% at 1200 °C, even close to the Cahill model's limited thermal conductivity at high temperature, which can be represented using Eq. (23)[74]:

$$\kappa_{Cahill}=\frac{k_B n^{2/3}(2v_t+v_l)}{2.48} \quad (23)$$

where k_B denotes the Boltzmann constant. According to Fig. 11(c), the $(8RE_{1/8})TaO_4$ ceramics exhibit a lower κ_{int} across the entire temperature range of 100–1200 °C than single-RE $RETaO_4$, YSZ, and $(Y_{1/5}Dy_{1/5}Sm_{1/5}Yb_{1/5}Er_{1/5})TaO_4$ [31] materials. Moreover, compared with that of single-RE $RETaO_4$, the κ_{int} of $(8RE_{1/8})TaO_4$ decreases by 19.2%–33.6% at 100 °C and 30.0%–31.1% at 1200 °C, indicating that the thermal conductivity of single-RE $RETaO_4$ is reduced by the high-entropy method. There is no fluctuation in size or mass in single-RE $RETaO_4$, but $(8RE_{1/8})TaO_4$ has high size disorder (4.136%–4.272%) and mass disorder (2.901%–2.950%), which is greater than that of most high-entropy four-, five- and six-component rare-earth materials, as shown in Table 3 [31,36]. Furthermore, the distortion degree (Δd_{tot}, %) of $(8RE_{1/8})TaO_4$ (1.2467%–2.7861%) is higher than those of single-RE $RETaO_4$ (0.1332%–0.3884%) and $(Y_{1/5}Dy_{1/5}Sm_{1/5}Yb_{1/5}Er_{1/5})TaO_4$ (1.0700%) [31], as shown in Table 5, and the results indicate that the lattice distortion is improved by the conformational entropy.

The phonon scattering mechanism of $(8RE_{1/8})TaO_4$ is analyzed by the Debye–Callaway model based on Eq. (24) [75]:

$$\kappa_l=\frac{k_B}{2\pi^2 v_m}\left(\frac{k_B T}{\hbar}\right)^3\int_0^{\theta_D/T}\tau_{tot}(x)\frac{x^4 e^x}{(e^x-1)^2}\mathrm{d}(x) \quad (24)$$

where $x=\hbar\omega/k_B T$; $\hbar$ and ω correspond to the Plank constant and phonon angular frequency, respectively. The total phonon relaxation time (τ_{tot}^{-1}) is a reciprocal sum of Umklapp processes (τ_U^{-1}), point defects (τ_{PD}^{-1}), grain boundaries (τ_{GB}^{-1}), domain boundaries (τ_{DB}^{-1}), dislocation strains (τ_{DS}^{-1}), and dislocation cores (τ_{DC}^{-1}). The relaxation time for phonon scattering calculated according to the Debye model is shown in Fig. 12(a), and the parameters are listed in Table 7. First, the relaxation time associated with Umklapp phonon-phonon scattering τ_U is calculated from Eq. (25) [68,76]:

$$\tau_U^{-1}=\frac{2}{(6\pi^2)^{1/3}}\frac{k_B\overline{V}^{1/3}\gamma^2\omega^3 T}{\overline{M}v_m^3} \quad (25)$$

where $\overline{V}$ is the average atomic volume; T is the temperature; $\overline{M}$ is the average atomic mass. Phonon-phonon scattering ($\tau_U^{-1}\infty\omega^3$) is typically the major scattering effect at temperatures above θ_D. Second, Eqs. (26) and (27) can be used to predict grain boundary and domain boundary scattering in polycrystalline materials with a grain size of d_{GB} and domain width of d_{DB} [76,77]:

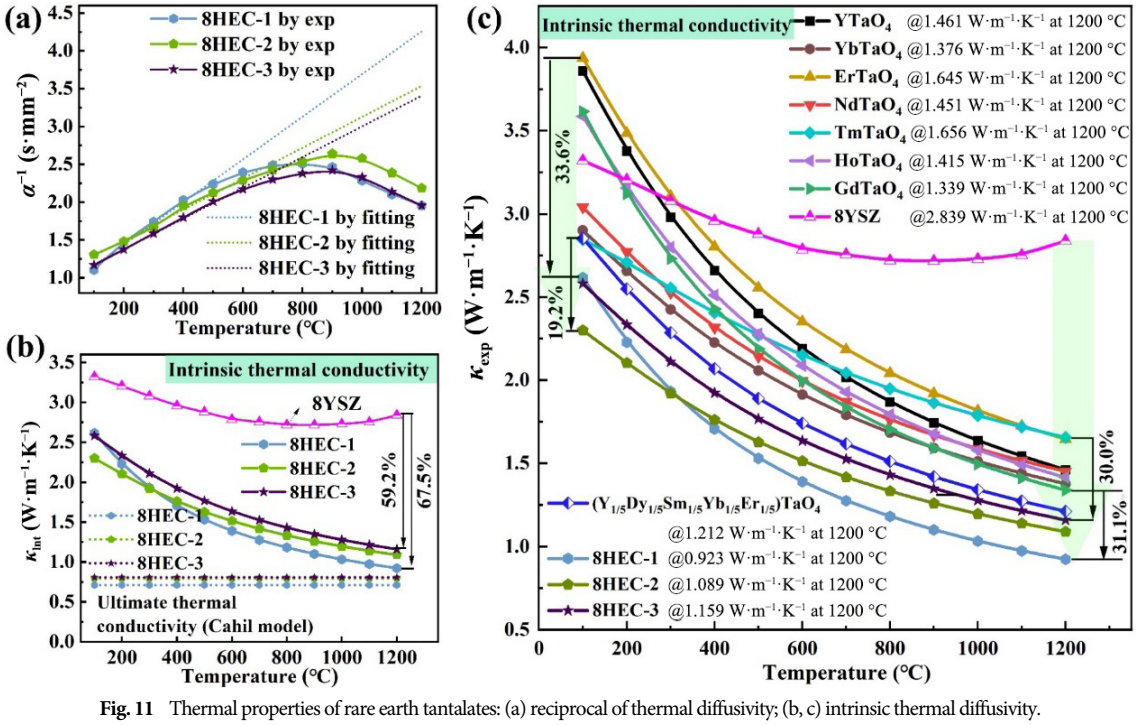

Fig. 11 Thermal properties of rare earth tantalates: (a) reciprocal of thermal diffusivity; (b, c) intrinsic thermal diffusivity.

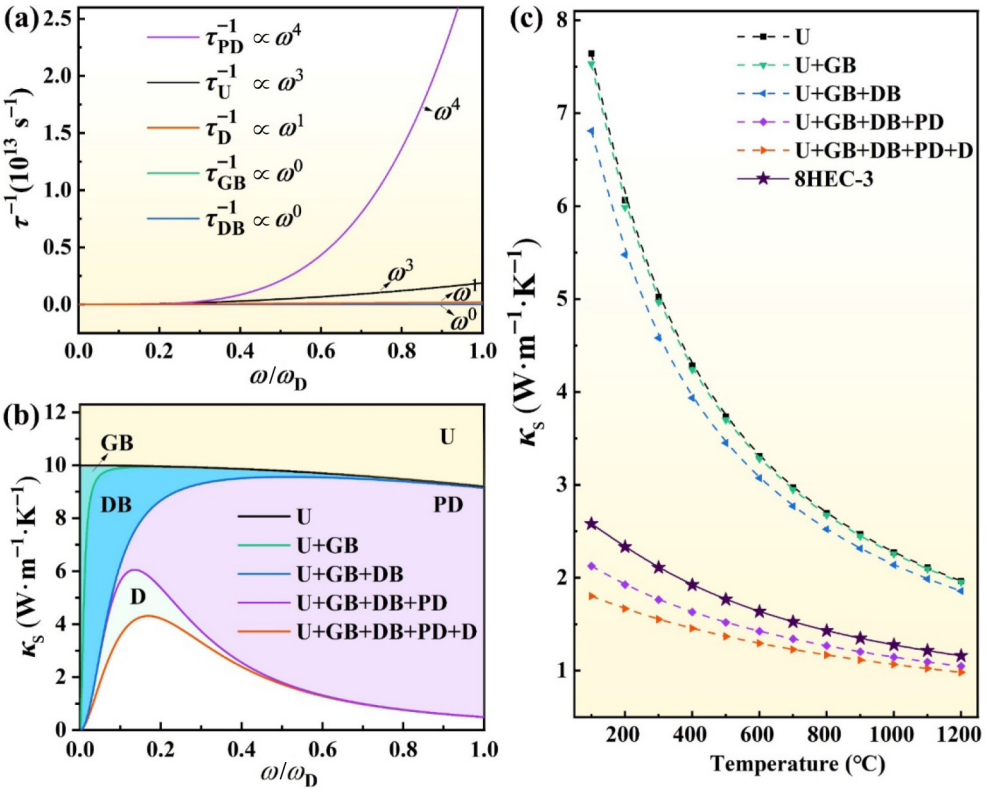

Fig. 12 Thermal transport properties of 8HEC-3 with various phonon scattering processes as described by the Debye–Callaway model: (a) dependence of phonon relaxation times on angular frequency; (b) spectral lattice thermal conductivity, including Umklapp scattering (U), grain boundary scattering (GB), domain boundary scattering (DB), point defect scattering (PD), and dislocation scattering (D); (c) fitted lattice thermal conductivity.

Table 7 Key parameters of 8HEC-3 for Debye–Callaway modeling

Parameter	Note	Value
θ_D	Acoustic mode Debye temperature	290 K
$\overrightarrow{V}$	Average atomic volume	5.37×10^{-30} m^3
$\overleftarrow{M}$	Average atomic mass	1.10×10^{-25} kg
γ	Grüneisen parameter	1.65
d_{GB}	Grain size	9.62 μm
d_{PB}	Domain boundary width	20.2 nm
A	Domain boundary fitting parameter	0.1
Γ	Point defect scattering parameter	0.37
N_D	Dislocation density	1.16×10^{14} cm^{-2}
B_D	Magnitude of Burger's vector	5.1 nm
ξ	Poisson's ratio	0.28
v_l	Longitudinal sound velocity	3638 m·s^{-1}
v_t	Transverse sound velocity	2012 m·s^{-1}
v_m	Average speed of sound	2242 m·s^{-1}
D	Mass density	8967 kg·m^{-3}

$$\tau_{GB}^{-1} = \frac{v_m}{d_{GB}} \tag{26}$$

$$\tau_{DB}^{-1} = A\frac{v_m}{d_{DB}} \tag{27}$$

Grain boundary and domain boundary scattering ($\tau_{GB}^{-1}\propto\omega^O$, $\tau_{DB}^{-1}\propto\omega^0$) is more effective at targeting low-frequency phonons than Umklapp scattering [78]. As shown in Figs. 4 and 9, domain boundaries within the grains increase the number of boundaries and contribute to reducing the thermal conductivity at low temperatures. Third, the following simplified dislocations are used to calculate the dislocation contribution to the relaxation time (Eqs. (28) and (29)) [76]:

$$\tau_{DC}^{-1} = N_D\frac{\overline{V}^{4/3}\omega^3}{v_m^2} \tag{28}$$

$$\tau_{DS}^{-1} = 0.6\times B_D^2 N_D \gamma^2 \omega \left\{\frac{1}{2}+\frac{1}{24}\left(\frac{1-2\xi}{1-\xi}\right)^2\left[1+\sqrt{2}\left(\frac{v_l}{v_t}\right)^2\right]^2\right\} \tag{29}$$

where N_D denotes the dislocation density; B_D is the magnitude of the Burgers vector of the dislocation; τ_{DC} denotes that the dislocation core plays a dominant role; while τ_{DS} is the dislocation-induced strain field that plays a key role. Figure 9(a) shows the dislocation lines of 8HEC-3, and the occurrence of periodic dislocations resulting from low-energy grain boundaries introduces a novel mechanism that affects low- to mid-frequency phonons, leading to a significant reduction in the lattice thermal conductivity [68]. This mechanism is dependent on both $\tau_{DC}^{-1}\propto\omega^3$ and $\tau_{DS}^{-1}\propto\omega^1$, which lies between the dependency for point defects and boundary scattering [68,76]. Finally, the phenomenon of scattering caused by point defects is a result of both mass and strain variations within the lattice structure. Here, Eq. (30) represents the point defect contribution to the relaxation time [68,79]:

$$\tau_{PD}^{-1} = \frac{\overline{V}\omega^4}{4\pi\, v_m{}^3}\Gamma \tag{30}$$

The XPS data in Fig. 2(c) demonstrate the existence of oxygen vacancies in $(8RE_{1/8})TaO_4$. High-frequency phonon scattering ($\tau_{PD}^{-1}\propto\omega^4$) is the primary target of point defects. The utilization of point defect scattering has proven to be effective in the application

of thermal barrier coatings, such as yttria stabilized zirconia (YSZ) [80].

As shown in Fig. 12(b), the predominant scattering effect is typically Umklapp phonon–phonon scattering. The second factor is the greater contribution of point defects to phonon scattering. Grain and domain scatterings are mainly for low-frequency phonon scattering, but the number of domain boundaries greatly exceeds that of grain boundaries, resulting in a greater contribution to phonon scattering than that of the grain boundaries. Dislocations mainly scatter low-frequency phonons, indicating that the dislocation-induced strain field plays a key role rather than the dislocation core. Furthermore, the lattice thermal conductivity κ_l of $(Y_{1/8}Dy_{1/8}Lu_{1/8}Yb_{1/8}Er_{1/8}Sm_{1/8}–Nd_{1/8}Tm_{1/8})TaO_4$ (8HEC-3) under various types of phonon scattering was calculated using the Debye–Callaway model, as shown in Fig. 12(c). The predicted κ_l curve approximately matches the intrinsic thermal conductivity of 8HEC-3, suggesting that the large contribution of multiscale lattice defects increases phonon scattering and decreases the thermal conductivity.

4.3 Mechanism of ultra-low oxygen ion conductivity

Owing to the significant impact of porosity on the ionic conductivities of sintered samples, the ionic conductivities of samples were normalized by following the effective medium theory (Eq. (31) [81,82]:

$$\sigma' = \sigma\frac{1+\varphi/2}{1-\varphi} \tag{31}$$

where σ denotes the ionic conductivity of porous samples; σ' is the ionic conductivity of fully dense samples; and φ is the porosity. The corrected results are plotted in Figs. 13(a) and 13(b). Furthermore, Table 8 shows that the ionic conductivities of single-RE $RETaO_4$ and $(8RE_{1/8})TaO_4$ are much lower than those of other T/EBCs, including RE_3NbO_7 [22], $RE_2Zr_2O_7$ [23], $RE_4Zr_3O_{12}$ [13], and $RE_2Ce_2O_7$ [24], indicating that rare earth tantalate has better oxygen barrier performance.

As shown in Fig. 13(c), the ionic conductivity of single-RE $RETaO_4$ and $(8RE_{1/8})TaO_4$ is 851–29,667 times less than that of 8YSZ at 900 °C. The essential reason for the low ionic conductivity of tantalates is that they have high bond strength. The bonding strength is negatively correlated with the bond length and is primarily responsible for determining the stability of the crystal structure and the ability of oxygen to escape. The average bond length of RE–O is much longer than that of Ta–O in Table 5, indicating that Ta–O dominates the bonding strength in $(8RE_{1/8})TaO_4$. Meanwhile, Fig. 13(d) shows that the average

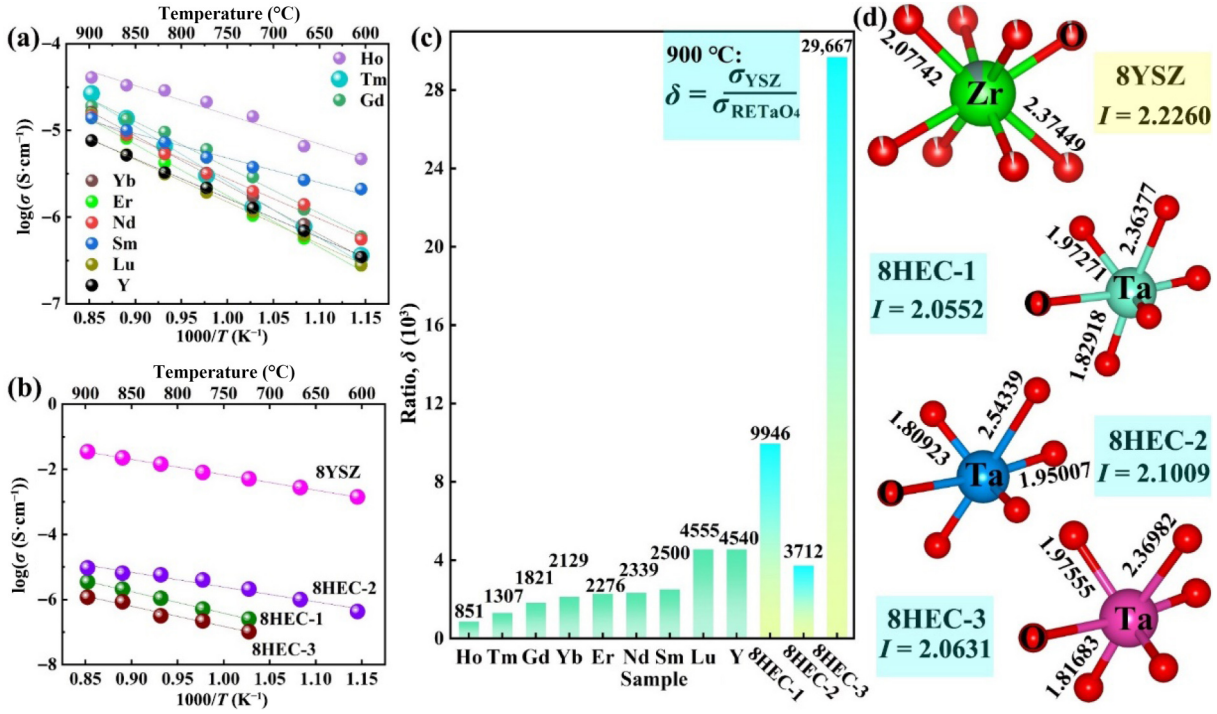

Fig. 13 Ionic conductivity: (a) single-RE $RETaO_4$; (b) $(8RE_{1/8})TaO_4$ and 8YSZ; (c) ionic conductivity ratio of 8YSZ to single-RE $RETaO_4$ and $(8RE_{1/8})TaO_4$; and (d) comparison of bond lengths of Ta–O and Zr–O.

Table 8 Logarithmic oxygen ion conductivity $\log(\sigma\,(S{\cdot}cm^{-1}))$ of various TBCs at different temperatures

Sample	600 °C	650 °C	700 °C	750 °C	800 °C	850 °C	900 °C
$(5RE_{0.2})_2Ce_2O_7$ [24]	−3.25	−2.90	−2.59	−2.30	—	—	—
$Nd_2Zr_2O_7$ [23]	−1.45	−1.32	−1.21	−1.11	−1.03	−0.96	−0.87
$Dy_3Nb_3O_7$ [22]	−2.39	−2.21	−2.04	—	—	—	—
$Zr_3Gd_4O_{12}$ [13]	−4.12	−3.78	−3.42	—	—	—	—
8YSZ	−2.85	−2.56	−2.29	−2.10	−1.84	−1.65	−1.46
8HEC-1	—	—	−6.60	−6.29	−5.96	−5.68	−5.46
8HEC-2	−6.37	−6.00	−5.68	−5.40	−5.24	−5.19	−5.03
8HEC-3	—	—	−6.99	−6.66	−6.50	−6.07	−5.93

bond lengths of Ta–O in $(8RE_{1/8})TaO_4$ are all lower than those of Zr–O in 8YSZ, indicating that $(8RE_{1/8})TaO_4$ has a stronger bonding strength and that the oxygen atoms or oxygen vacancies centered on the Ta atoms do not easily escape to become carriers; therefore, $(8RE_{1/8})TaO_4$ has a lower ionic conductivity than 8YSZ. Additionally, the distorted lattice increases the probability of carrier collisions with multicomponent cations and thereby reduces the carrier migration rate, leading to a lower ionic conductivity for high-entropy $(8RE_{1/8})TaO_4$.

The ionic conductivity is also inversely proportional to activation energy, according to Eq. (11). The larger the activation energy, the larger the energy required for oxygen ion migration, and the lower the ionic conductivity under the same conditions. Figure 14 shows the Arrhenius plot and activation energy of single-RE $RETaO_4$, $(8RE_{1/8})TaO_4$, and 8YSZ. $(8RE_{1/8})TaO_4$ and single-RE $RETaO_4$ have similar activation energies, which are higher than those of 8YSZ except $SmTaO_4$ and $HoTaO_4$; this may be the result of different phase structures with various oxygen transport barriers.

There is also significant variation in the oxygen ion conductivity among the three high-entropy samples for the following reasons. Oxygen vacancies act as carriers for hopping of oxygen ions, and the oxygen ion conductivity is proportional to the oxygen vacancy concentration based on Eq. (32) [83]:

$$\sigma = e\mu V_{\ddot{O}} \tag{32}$$

where μ is the mobility and e is the effective charge. However, when the oxygen vacancy concentration exceeds the threshold, dopant–vacancy binding and vacancy–vacancy interactions in samples may lead to a decrease in the concentration of mobile oxygen vacancies; that is, many oxygen vacancies form clusters that hinder the migration of oxygen ions, leading to a decrease in oxygen ion conductivity [84,85]. As shown in Fig. 15, the oxygen ion conductivity decreases with increasing oxygen vacancy concentration because the aggregation of oxygen vacancies in the eight-component rare earth tantalate results in the formation of oxygen vacancy clusters that impede the migration of oxygen ions.

5 Conclusions

In this study, the high-entropy component $(8RE_{1/8})TaO_4$ determined by size disorder (4.136%–4.272%) and mass disorder (2.901%–2.950%) was successfully synthesized via spark plasma sintering. As shown in Fig. 16, the eight-component rare-earth

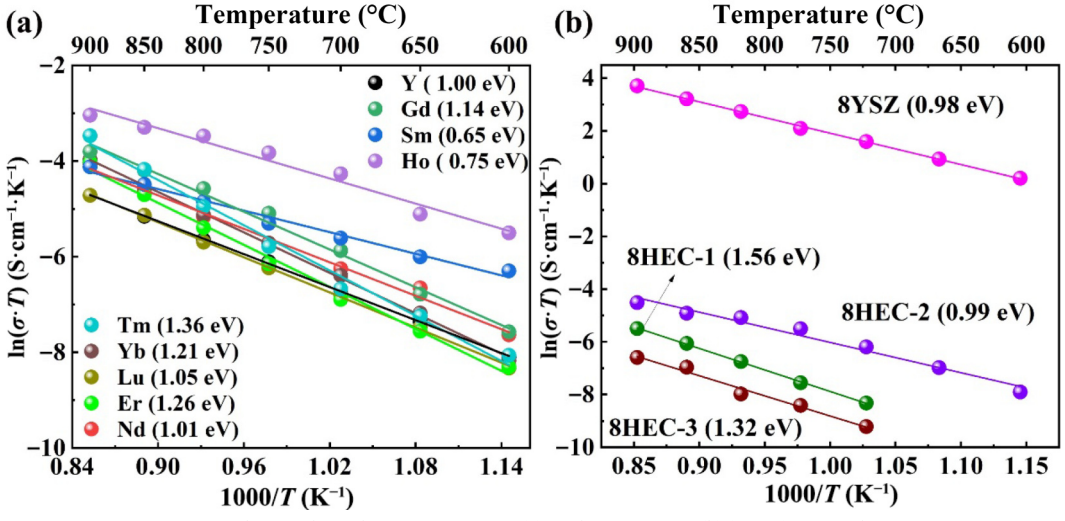

Fig. 14 Arrhenius plot and activation energies: (a) single-RE $RETaO_4$; (b) $(8RE_{1/8})TaO_4$ and 8YSZ.

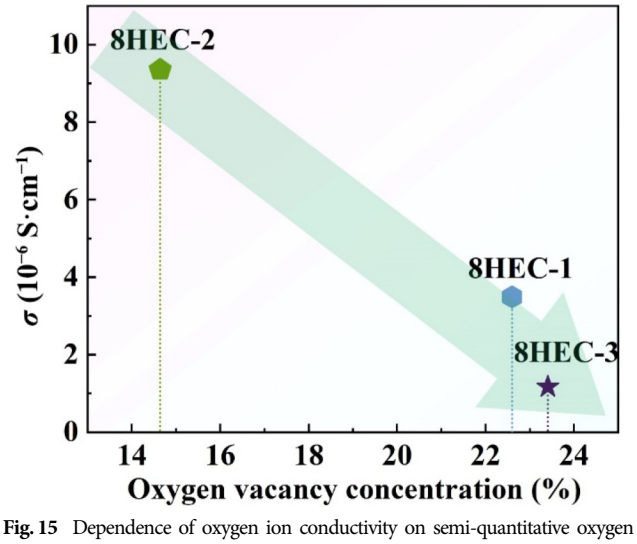

Fig. 15 Dependence of oxygen ion conductivity on semi-quantitative oxygen vacancy concentration fitted by O 1s XPS peak.

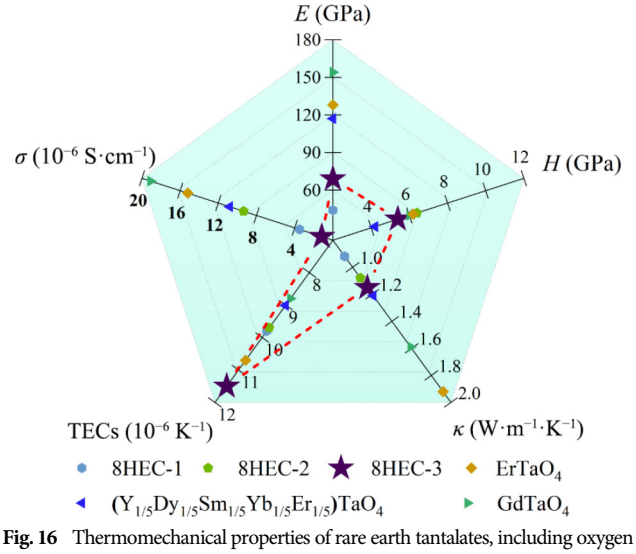

Fig. 16 Thermomechanical properties of rare earth tantalates, including oxygen ionic conductivity σ (10^{-6} S·cm^{-1}), thermal conductivity κ (W·m^{-1}·K^{-1}), Young's modulus E (GPa), thermal expansion coefficient TECs (10^{-6} K^{-1}), and hardness H (GPa).

tantalate $(8RE_{1/8})TaO_4$ exhibits superior thermodynamic properties compared with the single-RE $RETaO_4$ and $(Y_{1/5}Dy_{1/5}Sm_{1/5}Yb_{1/5}Er_{1/5})TaO_4$; among them, 8HEC-3 possesses an extremely low oxygen-ionic conductivity (1.17×10^{-6} S·cm^{-1}@900 °C), thermal conductivity (1.15 W·m^{-1}·K^{-1}@1200 °C), Young's modulus (69 GPa), a high coefficient of thermal expansion (11.5×10^{-6} K^{-1}@1200 °C), and hardness (5.1 GPa). In addition, Umklapp processes, grain boundaries, domain boundaries, dislocations, vacancy defects and $(8RE_{1/8})TaO_4$ enhance phonon scattering, leading to low thermal conductivity. Moreover, compared with 8YSZ, the low ionic conductivity of $(8RE_{1/8})TaO_4$ benefits from the strong Ta–O bonding strength, large number of oxygen vacancy clusters, and severe lattice distortions that impede carrier transport.

Acknowledgements

This research was supported by the National Natural Science Foundation of China (No. 52402077), the Open Project of Shaanxi Laboratory (No. 2021SXSYS-01-05), the Open Project of Yunnan Precious Metals Laboratory (No. YPML-2023050240), and the Yunnan Fundamental Research Projects (Nos. 202201BE070001-008, 202201AT070192, and 202101BE070001-011).

Declaration of competing interest

The authors have no competing interests to declare that are relevant to the content of this article. The author Jing Feng is the Editorial Committee member of this journal.

Electronic Supplementary Material

Supplementary material is available in the online version of this article at https://doi.org/10.26599/JAC.2024.9221000.

References

[1] Padture NP, Gell M, Jordan EH. Thermal barrier coatings for gas-turbine engine applications. *Science* 2002, **296**: 280–284.

[2] Wei ZY, Meng GH, Chen L, *et al.* Progress in ceramic materials and structure design toward advanced thermal barrier coatings. *J Adv Ceram* 2022, **11**: 985–1068.

[3] Daroonparvar M, Yajid MAM, Yusof NM, *et al.* Effect of Y_2O_3 stabilized ZrO_2 coating with tri-model structure on bi-layered thermally grown oxide evolution in nano thermal barrier coating systems at elevated temperatures. *J Rare Earths* 2014, **32**: 57–77.

[4] Zhang PX, Duan XJ, Xie XC, *et al.* Xenotime-type high-entropy $(Dy_{1/7}Ho_{1/7}Er_{1/7}Tm_{1/7}Yb_{1/7}Lu_{1/7}Y_{1/7})PO_4$: A promising thermal/environmental barrier coating material for SiC_f/SiC ceramic matrix composites. *J Adv Ceram* 2023, **12**: 1033–1045.

[5] Wang J, Li JY, Jiang CY, *et al.* Advanced rare earth tantalate $RETaO_4$ (RE = Dy, Gd and Sm) with excellent oxygen/thermal barrier performance. *J Rare Earths* 2024, **42**: 1595–1603.

[6] Evans AG, He MY, Hutchinson JW. Mechanics-based scaling laws for the durability of thermal barrier coatings. *Prog Mater Sci* 2001, **46**: 249–271.

[7] Tolpygo VK, Clarke DR. Surface rumpling of a (Ni, Pt)Al bond coat induced by cyclic oxidation. *Acta Mater* 2000, **48**: 3283–3293.

[8] Arnal S, Fourcade S, Mauvy F, *et al.* Design of a new yttrium silicate Environmental Barrier Coating (EBC) based on the relationship between microstructure, transport properties and protection efficiency. *J Eur Ceram Soc* 2022, **42**: 1061–1076.

[9] Dai MQ, Song XM, Lin CC, *et al.* Investigation of microstructure changes in Al_2O_3–YSZ coatings and YSZ coatings and their effect on thermal cycle life. *J Adv Ceram* 2022, **11**: 345–353.

[10] Wang J, Song JB, Jiang CY, *et al.* Rare earth tantalate coating materials for thermal and oxidation protection of carbon–carbon composites. *Ceram Int* 2024, **50**: 26703–26714.

[11] Wang R, Dong TS, Di YL, *et al.* High temperature oxidation resistance and thermal growth oxides formation and growth mechanism of double-layer thermal barrier coatings. *J Alloys Compd* 2019, **798**: 773–783.

[12] Wang SQ, Ye ZY, Ge YL, *et al.* High temperature oxidation behavior at 1250 °C: A new multilayer modified silicide coating design strategy on niobium alloys. *J Mater Sci Technol* 2025, **210**: 159–169.

[13] Zhao M, Pan W, Li TJ, *et al.* Oxygen-vacancy-mediated microstructure and thermophysical properties in $Zr_3Ln_4O_{12}$ for high-temperature applications. *J Am Ceram Soc* 2019, **102**: 1961–1970.

[14] Lee KN. $Yb_2Si_2O_7$ Environmental barrier coatings with reduced bond coat oxidation rates *via* chemical modifications for long life. *J Am Ceram Soc* 2019, **102**: 1507–1521.

[15] Zhang HY, Liu ZW, Yang XB, *et al.* Interface failure behavior of YSZ thermal barrier coatings during thermal shock. *J Alloys Compd* 2019, **779**: 686–697.

[16] Daroonparvar M, Yajid MAM, Yusof NM, *et al.* Investigation of three steps of hot corrosion process in Y_2O_3 stabilized ZrO_2 coatings including nano zones. *J Rare Earths* 2014, **32**: 989–1002.

[17] Rajeswari K, Suresh MB, Hareesh US, *et al.* Studies on ionic conductivity of stabilized zirconia ceramics (8YSZ) densified through conventional and non-conventional sintering methodologies. *Ceram Int* 2011, **37**: 3557–3564.

[18] Moskal G, Mikuśkiewicz M. Microstructure and thermal conductivity characteristics of $Sm_2Zr_2O_7$+8YSZ type TBCs. *Defect Diffus Forum* 2013, **336**: 91–96.

[19] Lipkin DM, Krogstad JA, Gao Y, *et al.* Phase evolution upon aging of air-plasma sprayed *t*'-zirconia coatings: I—Synchrotron X-ray diffraction. *J Am Ceram Soc* 2013, **96**: 290–298.

[20] VanValzah JR, Eaton HE. Cooling rate effects on the tetragonal to monoclinic phase transformation in aged plasma-sprayed yttria partially stabilized zirconia. *Surf Coat Tech* 1991, **46**: 289–300.

[21] Tian ZL, Zheng LY, Wang JM, *et al.* Theoretical and experimental determination of the major thermo-mechanical properties of RE_2SiO_5 (RE = Tb, Dy, Ho, Er, Tm, Yb, Lu, and Y) for environmental and thermal barrier coating applications. *J Eur Ceram Soc* 2016, **36**: 189–202.

[22] Yang J, Pan W, Han Y, *et al.* Mechanical properties, oxygen barrier property, and chemical stability of RE_3NbO_7 for thermal barrier coating. *J Am Ceram Soc* 2020, **103**: 2302–2308.

[23] Yamamura H, Nishino H, Kakinuma K, *et al.* Electrical conductivity anomaly around fluorite–pyrochlore phase boundary. *Solid State Ion* 2003, **158**: 359–365.

[24] Ping XY, Meng B, Li C, *et al.* Thermophysical and electrical properties of rare-earth-cerate high-entropy ceramics. *J Am Ceram Soc* 2022, **105**: 4910–4920.

[25] Wang J, Chong XY, Zhou R, *et al.* Microstructure and thermal properties of $RETaO_4$ (RE = Nd, Eu, Gd, Dy, Er, Yb, Lu) as promising thermal barrier coating materials. *Scripta Mater* 2017, **126**: 24–28.

[26] Chen L, Hu MY, Wu P, *et al.* Thermal expansion performance and intrinsic lattice thermal conductivity of ferroelastic $RETaO_4$ ceramics. *J Am Ceram Soc* 2019, **102**: 4809–4821.

[27] Chen L, Li BH, Feng J. Rare-earth tantalates for next-generation thermal barrier coatings. *Prog Mater Sci* 2024, **144**: 101265.

[28] Wang J, Zhou Y, Chong XY, *et al.* Microstructure and thermal properties of a promising thermal barrier coating: $YTaO_4$. *Ceram Int* 2016, **42**: 13876–13881.

[29] Chen L, Hu MY, Wang JK, *et al.* Dominant mechanisms of thermo-mechanical properties of weberite-type RE_3TaO_7 (RE = La, Pr, Nd, Eu, Gd, Dy) tantalates toward multifunctional thermal/environmental barrier coating applications. *Acta Mater* 2024, **270**: 119857.

[30] Chen L, Jiang YH, Chong XY, *et al.* Synthesis and thermophysical properties of $RETa_3O_9$ (RE = Ce, Nd, Sm, Eu, Gd, Dy, Er) as

promising thermal barrier coatings. *J Am Ceram Soc* 2018, **101**: 1266–1278.
[31] Wang J, Jin QQ, Song JB, *et al.* Revealing the low thermal conductivity of high-entropy rare-earth tantalates via multi-scale defect analysis. *J Adv Ceram* 2023, **12**: 2087–2100.
[32] Wang J, Chong XY, Lv L, *et al.* High-entropy ferroelastic (10$RE_{0.1}$)TaO_4 ceramics with oxygen vacancies and improved thermophysical properties. *J Mater Sci Technol* 2023, **157**: 98–106.
[33] Gurunathan R, Hanus R, Dylla M, *et al.* Analytical models of phonon–point-defect scattering. *Phys Rev Applied* 2020, **13**: 034011.
[34] Wright AJ, Wang QY, Ko ST, *et al.* Size disorder as a descriptor for predicting reduced thermal conductivity in medium- and high-entropy pyrochlore oxides. *Scripta Mater* 2020, **181**: 76–81.
[35] Shannon RD. Revised effective ionic radii and systematic studies of interatomic distances in halides and chalcogenides. *Acta Cryst A* 1976, **32**: 751–767.
[36] Zhu JT, Lou ZH, Zhang P, *et al.* Preparation and thermal properties of rare earth tantalates ($RETaO_4$) high-entropy ceramics. *J Inorg Mater* 2021, **36**: 411.
[37] Chong XY, Palma JPS, Wang Y, *et al.* Thermodynamic properties of the Yb–Sb system predicted from first-principles calculations. *Acta Mater* 2021, **217**: 117169.
[38] Wang J, Jin QQ, Song JB, *et al.* Multiscale defect-mediated thermophysical properties of high-entropy ferroelastic rare-earth tantalates. *Ceram Int* 2023, **49**: 40019–40030.
[39] Shang SL, Wang Y, Kim D, *et al.* First-principles thermodynamics from phonon and Debye model: Application to Ni and Ni_3Al. *Comp Mater Sci* 2010, **47**: 1040–1048.
[40] Wang SQ, Ye ZY, Zhang HP, *et al.* High-entropy strategy for high-temperature broadband infrared radiation and low thermal conductivity. *Ceram Int* 2024, **50**: 18806–18813.
[41] Leitner J, Voňka P, Sedmidubský D, *et al.* Application of Neumann–Kopp rule for the estimation of heat capacity of mixed oxides. *Thermochim Acta* 2010, **497**: 7–13.
[42] Mukherjee R, Ghosh B, Saha S, *et al.* Structural and electrical transport properties of a rare earth double perovskite oxide: Ba_2ErNbO_6. *J Rare Earths* 2014, **32**: 334–342.
[43] Xiang HM, Xing Y, Dai FZ, *et al.* High-entropy ceramics: Present status, challenges, and a look forward. *J Adv Ceram* 2021, **10**: 385–441.
[44] Sun ZG, Li JG, Qian HY, *et al.* Optical grade $(Gd_{0.95-x}Lu_xEu_{0.05})_3Al_5O_{12}$ ceramics with near-zero optical loss: Effects of Lu^{3+} doping on structural feature, microstructure evolution, and far-red luminescence. *J Adv Ceram* 2024, **13**: 113–123.
[45] Qu CK, Chen L, Lv L, *et al.* Low thermal conductivity and anisotropic thermal expansion of ferroelastic $(Gd_{1-x}Y_x)TaO_4$ ceramics. *J Adv Ceram* 2022, **11**: 1696–1713.
[46] Cong HJ, Zhang HJ, Wang JY, *et al.* Structural and thermal properties of the monoclinic Lu_2SiO_5 single crystal: Evaluation as a new laser matrix. *J Appl Crystallogr* 2009, **42**: 284–294.
[47] Korkos S, Xanthopoulos NJ, Botzakaki MA, *et al.* XPS analysis and electrical conduction mechanisms of atomic layer deposition grown Ta_2O_5 thin films onto p-Si substrates. *J Vac Sci Technol A* 2020, **38**: 032402.
[48] Simpson R, White RG, Watts JF, *et al.* XPS investigation of monatomic and cluster argon ion sputtering of tantalum pentoxide. *Appl Surf Sci* 2017, **405**: 79–87.
[49] Frankcombe TJ, Liu Y. Interpretation of oxygen 1s X-ray photoelectron spectroscopy of ZnO. *Chem Mater* 2023, **35**: 5468–5474.
[50] Xiang XM, Zhao HH, Yang J, *et al.* Promoting effect of KIT-6 to support Ni–$Ce_{0.8}Gd_{0.2}O_{2-\delta}$ as efficient coke-resistant catalysts for carbon dioxide reforming of methane. *Eur J Inorg Chem* 2020, **2020**: 631–637.
[51] Lou ZH, Zhang P, Zhu JT, *et al.* A novel high-entropy perovskite ceramics $Sr_{0.9}La_{0.1}(Zr_{0.25}Sn_{0.25}Ti_{0.25}Hf_{0.25})O_3$ with low thermal conductivity and high Seebeck coefficient. *J Eur Ceram Soc* 2022, **42**: 3480–3488.
[52] Wang XX, Zhou DY, Li SD, *et al.* Ferroelectric yttrium doped hafnium oxide films from all-inorganic aqueous precursor solution. *Ceram Int* 2018, **44**: 13867–13872.
[53] Wang J, Zheng Q, Shi XL, *et al.* Microstructural evolution and thermal–physical properties of $YTaO_4$ coating after high-temperature exposure. *Surf Coat Tech* 2023, **456**: 129222.
[54] Virkar AV, Matsumoto RLK. Ferroelastic domain switching as a toughening mechanism in tetragonal zirconia. *J Am Ceram Soc* 1986, **69**: C-224–C-226.
[55] Shian S, Sarin P, Gurak M, *et al.* The tetragonal–monoclinic, ferroelastic transformation in yttrium tantalate and effect of zirconia alloying. *Acta Mater* 2014, **69**: 196–202.
[56] Lepple M, Ushakov SV, Lilova K, *et al.* Thermochemistry and phase stability of the polymorphs of yttrium tantalate, $YTaO_4$. *J Eur Ceram Soc* 2021, **41**: 1629–1638.
[57] Wu P, Zhou YX, Wu FS, *et al.* Theoretical and experimental investigations of mechanical properties for polymorphous $YTaO_4$ ceramics. *J Am Ceram Soc* 2019, **102**: 7656–7664.
[58] Liu B, Liu YC, Zhu CH, *et al.* Advances on strategies for searching for next generation thermal barrier coating materials. *J Mater Sci Technol* 2019, **35**: 833–851.
[59] Mori M, Hiei Y, Sammes NM, *et al.* Thermal-expansion behaviors and mechanisms for Ca- or Sr-doped lanthanum manganite perovskites under oxidizing atmospheres. *J Electrochem Soc* 2000, **147**: 1295.
[60] Wang JX, Li LP, Campbell BJ, *et al.* Structure, thermal expansion and transport properties of $BaCe_{1-x}Eu_xO_{3-\delta}$ oxides. *Mater Chem Phys* 2004, **86**: 150–155.
[61] Chen XG, Sang WW, Guo YH, *et al.* Thermophysical performances of $(Er_{1-x}Yb_x)_3TaO_7$ oxides for high-temperature applications. *Ceram Int* 2022, **48**: 5674–5680.
[62] Wang SQ, Wang YM, Chen GL, *et al.* High-temperature broadband infrared radiation from rare earth monosilicate-based ceramics. *J Eur Ceram Soc* 2024, **44**: 6510–6517.
[63] Wang SQ, Zhang HP, Wang YM, *et al.* Doping engineering for high-temperature broadband high emissivity and low thermal conductivity of ytterbium chromate-based ceramics. *Ceram Int* 2024, **50**: 17657–17664.
[64] Sanditov DS, Belomestnykh VN. Relation between the parameters of the elasticity theory and averaged bulk modulus of solids. *Tech Phys* 2011, **56**: 1619–1623.
[65] Kawamura M, Asakura M, Okamoto NL, *et al.* Plastic deformation of single crystals of the equiatomic Cr–Mn–Fe–Co–Ni high-entropy alloy in tension and compression from 10 K to 1273 K. *Acta Mater* 2021, **203**: 116454.
[66] Zhang S, Wang XH, Zhang C, *et al.* Microstructure, elastic/mechanical and thermal properties of $CrTaO_4$: A new thermal barrier material. *J Adv Ceram* 2024, **13**: 373–387.
[67] Ren XR, Pan W. Mechanical properties of high-temperature-degraded yttria-stabilized zirconia. *Acta Mater* 2014, **69**: 397–406.
[68] Kim SI, Lee KH, Mun HA, *et al.* Dense dislocation arrays embedded in grain boundaries for high-performance bulk thermoelectrics. *Science* 2015, **348**: 109–114.
[69] Samsonov GV. *The Oxide Handbook*. New York (USA): Springer Science & Business Media, 2013.
[70] Chandrasekharaiah M. Volatilities of Refractory Inorganic Compounds. In: *The Characterization of High Temperature Vapors*. Margrave JL, Ed. New York (USA): Wiley, 1967: 495–507.
[71] Schulz U, Saruhan B, Fritscher K, *et al.* Review on advanced EB-PVD ceramic topcoats for TBC applications. *Int J Appl Ceram Tec* 2004, **1**: 302–315.
[72] Stanek CR, Minervini L, Grimes RW. Nonstoichiometry in $A_2B_2O_7$ pyrochlores. *J Am Ceram Soc* 2002, **85**: 2792–2798.
[73] Liu DB, Shi BL, Geng LY, *et al.* High-entropy rare-earth zirconate

ceramics with low thermal conductivity for advanced thermal-barrier coatings. *J Adv Ceram* 2022, **11**: 961–973.
[74] Cahill DG, Watson SK, Pohl RO. Lower limit to the thermal conductivity of disordered crystals. *Phys Rev B* 1992, **46**: 6131–6140.
[75] Callaway J. Model for lattice thermal conductivity at low temperatures. *Phys Rev* 1959, **113**: 1046–1051.
[76] Toberer ES, Zevalkink A, Snyder GJ. Phonon engineering through crystal chemistry. *J Mater Chem* 2011, **21**: 15843–15852.
[77] Yang TY, Gu SW, Zhang YX, *et al*. Pseudopolymorphic phase engineering for improved thermoelectric performance in copper sulfides. *Adv Mater* 2024, **36**: 2308353.
[78] Zhu JT, Xu J, Zhang P, *et al*. Enhanced mechanical and thermal properties of ferroelastic high-entropy rare-earth-niobates. *Scripta Mater* 2021, **200**: 113912.
[79] Chung JD, McGaughey AJH, Kaviany M. Role of phonon dispersion in lattice thermal conductivity modeling. *J Heat Transfer* 2004, **126**: 376–380.
[80] Klemens PG, Gell M. Thermal conductivity of thermal barrier coatings. *Mater Sci Eng A* 1998, **245**: 143–149.
[81] Petric A, Ling H. Electrical conductivity and thermal expansion of spinels at elevated temperatures. *J Am Ceram Soc* 2007, **90**: 1515–1520.
[82] Ping XY, Meng B, Yu XH, *et al*. Structural, mechanical and thermal properties of cubic bixbyite-structured high-entropy oxides. *Chem Eng J* 2023, **464**: 142649.
[83] Asadikiya M, Zhong Y. Oxygen ion mobility and conductivity prediction in cubic yttria-stabilized zirconia single crystals. *J Mater Sci* 2018, **53**: 1699–1709.
[84] Burbano M, Norberg ST, Hull S, *et al*. Oxygen vacancy ordering and the conductivity maximum in Y_2O_3-doped CeO_2. *Chem Mater* 2012, **24**: 222–229.
[85] Marrocchelli D, Bishop SR, Tuller HL, *et al*. Understanding chemical expansion in non-stoichiometric oxides: Ceria and zirconia case studies. *Adv Funct Mater* 2012, **22**: 1958–1965.